Thesis for the degree of Doctor of
Philosophy
in the Natural Sciences

The effect of site-specific mutations on hIAPP fibril polymorphism: A cryo-EM study towards potential inhibitors

---

Saik Ann Ooi

UNIVERSITY OF GOTHENBURG

Department of Chemistry and Molecular Biology
Gothenburg, 2024

Thesis for the degree of Doctor of Philosophy
in the Natural Sciences

The effect of site-specific mutations on hIAPP fibril polymorphism: A cryo-EM study towards potential inhibitors

Saik Ann Ooi

Cover: The PDB model of hIAPP-A25P polymorph 1 created with Pymol.

Copyright ©2024 by Saik Ann Ooi
ISBN 978-91-8069-595-4 (Print)
ISBN 978-91-8069-596-1 (PDF)
Available online at http://hdl.handle.net/2077/79240

Department of Chemistry and Molecular Biology
Division of Biochemistry and Structural Biology
University of Gothenburg
SE-405 30, Göteborg, Sweden
Printed by Stema Specialtryck AB
Borås, Sweden, 2024

SVANENMÄRKET
Trycksak
3041 0234

Abstract

The development of amyloid deposits in tissues, as a consequence of the self-assembly of misfolded proteins, is a critical pathological feature in a range of diseases, including neurodegenerative disorders and metabolic conditions such as diabetes. A comprehensive understanding of the mechanisms that drive this protein aggregation is essential for developing strategies capable of intervening in these disease processes and aiding in the creation of novel therapeutic approaches.

This thesis focuses on the aggregation of the human islet amyloid polypeptide (hIAPP), which plays a significant role in the progression of type 2 diabetes through the degeneration of the insulin-producing β-cells. The molecular basis of β-cell death associated with hIAPP aggregation remains poorly understood. One significant challenge is the rapid and intricate nature of amyloid fibril formation by hIAPP *in vitro*. Additionally, the application of traditional structural biology techniques to analyze this process proves difficult due to the structural complexity of the amyloid aggregates.

The environment of hIAPP has a strong effect on the aggregation, which has been investigated through papers I and III using ThT kinetics study and cryo-EM. The results indicated that buffers played a huge part in influencing the fibrils kinetics, distribution of fibrils on cryo-EM grids, and especially the fibril polymorphism.

In paper II, site-specific mutation has been carried out to evaluate the effect of proline on fibril formation. With the same proline mutation performed on three different sites, the results showed drastic changes in the kinetics. The molecular investigation using cryo-EM has shown that each mutant formed distinct polymorphic structures that were different from those published for wild-type IAPP. The results deliver insights into how the aggregation of hIAPP can be influenced through mutations.

Overall, this thesis contributes to our understanding of hIAPP aggregation *in vitro*, influenced by both mutations and co-aggregation. The insights gained from these studies are instrumental in advancing the development of therapeutic strategies aimed at disrupting or inhibiting amyloid aggregation pathways in a range of diseases, including type 2 diabetes.

Sammanfattning

Utvecklingen av amyloider i vävnader, som en konsekvens av självmontering av felvikta proteiner, är en kritisk patologisk egenskap vid olika sjukdomar, inklusive neurodegenerativa störningar och metabola tillstånd som diabetes. En omfattande förståelse av de mekanismer som driver denna proteinaggregering är avgörande för att utveckla strategier som kan ingripa i dessa sjukdomsprocesser och bidra till skapandet av nya mediciner.

Denna avhandling fokuserar på aggregeringen av det human islet amyloid polypeptide (hIAPP). hIAPP spelar en betydande roll i utveckling av typ 2-diabetes genome degeneration av de insulinproducerande β-cellerna. Den molekylära mekanism för β-cellens död i samband med hIAPP-aggregering förblir dåligt förstådd. En betydande utmaning är den snabba och intrikata naturen av amyloid fibrilbildning av hIAPP *in vitro*. Dessutom visar det sig att användningen av traditionella strukturella metoder för att analysera denna process är svårt på grund av den strukturella komplexiteten hos amyloidaggregeringarna.

Miljön för hIAPP har en stark effekt på aggregeringen, vilket har undersökts via papper I och III med hjälp av ThT-kinetikstudie och kryo-EM. Resultaten indikerade att buffertar spelade en stor roll i att påverka fibrillernas kinetik, distributionen av fibriller på kryo-EM-galler och särskilt fibrilpolymorfism.

I papper II har platsspecifik mutation genomförts för att utvärdera effekten av prolin på fibrilbildning. Med samma prolinmutation utförd på tre olika platser visade resultaten drastiska förändringar i kinetiken. Den molekylära undersökningen med hjälp av kryo-EM har visat att varje mutant bildade distinkta polymorfa strukturer som inte var liknande de publicerade strukturerna. Detta har gett insikt i hur aggregeringen av hIAPP kan påverkas genom mutationer.

Sammantaget bidrar denna avhandling till vår förståelse av hIAPP-aggregering *in vitro*, påverkad av både mutationer och samaggregation. Insikterna från dessa studier är instrumentella för att främja utvecklingen av terapeutiska strategier som syftar till att störa eller hämma amyloidaggregeringsvägarna vid olika sjukdomar, inklusive typ 2-diabetes.

Acknowledgements

This five years of PhD education has been a long journey, and it has finally come to an end. Completing a PhD during the pandemic was certainly not easy, and I have many people to be thankful for.

First, thank you to my supervisor, Michał, for choosing me as your first PhD student. The open-door policy that you have allowed me to pop by randomly for any questions. Even though it became Zoom when you moved to Uppsala, you still always answered my questions whenever I had one. The world of amyloid protein is wild, but having you around made it better. Your enthusiasm and passion made you a good supervisor. Alesia, my co-supervisor, thank you for being around whenever I need help, be it with peptides, HPLC, or random discussions. Sebastian and Gisela, my examiners, thank you for looking out for me and helping me out with some administrative work.

For people in Maj's group: Dylan, I am really glad that you joined our group; it was a great time working with you and sharing random ideas about what we should try on the projects (or whatnot). Himanshu, thank you for your helpfulness and all the random co-aggregation that you always wanted to try. Giorgio and Mikołaj, you guys made the group more fun, and all the best in your PhD studies. Joachim, thank you for helping me with lots of 2DIR questions and random programming whenever I needed it. Manoop, for helping me in the laser lab when it was needed.

To everyone else outside of Maj's group, thank you for helping me with everything in the lab when I was new in the division, by teaching and providing me assistance whenever there were things that I needed help with. I am not going to namedrop people, but thank you for coping with me for the whole duration of my PhD.

While there are many more people I would like to thank, I will keep the list short. The administrative people for helping with all aspects of the administration; Bruno and Lars, for all the computer technical support. I extend my gratitude to everyone at CCI, the Scilife cryo-EM facility, and the Umeå microscope facility for always being super helpful and friendly whenever I needed assistance with cryo-EM.

I am glad that I started my PhD in Lundberg, where everyone was welcoming and helped me out with various questions and assistance in the lab. To everyone that made Lundberg a fun place to be: the lunch topics, beer clubs, random fika around the corners, and not forgetting random spex filming without any explanations. To the people in Johannaberg, thanks for accompanying me while I was there running some experiments. While

Lundberg and Johannaberg are gone, I believe we will always cherish the moments we had. Toodaloo!

Publications

This thesis consists of the following research papers:

PAPER I: Dylan Valli*, **Saik Ann Ooi***, Giorgio Scattolini, Himanshu Chaudhary, Alesia A. Tietze, Michał Maj. Improving cryo-EM grids for amyloid fibrils using interface-active solutions and spectator proteins. Manuscript, under revision in Biophysical Journal.

PAPER II: **Saik Ann Ooi**, Dylan Valli, Mikołaj Kuska, Himanshu Chaudhary, Weixiao Yuan Wahlgren, Alesia A. Tietze, Sebastian Westenhoff, Michał Maj. High-resolution Cryo-EM analysis of the fibrils formed by the human Islet Amyloid Polypeptide containing site-specific proline mutations reveals diverse polymorphism and offers new insights for structure-based drug development. Manuscript.

PAPER III: Dylan Valli, **Saik Ann Ooi**, Himanshu Chaudhary, Alesia A. Tietze, Michał Maj. Solution composition regulates the inhibitory effect of rat IAPP on the human IAPP fibril formation. Manuscript.

---

*These authors contributed equally to the study.

Papers that I have contributed to but are not included in this thesis:

PAPER IV: Joachim Kübel, Giseong Lee, **Saik Ann Ooi**, Sebastian Westenhoff, Hogyu Han, Minhaeng Cho, and Michał Maj. (2019). Ultrafast Chemical Exchange Dynamics of Hydrogen Bonds Observed via Isonitrile Infrared Sensors: Implications for Biomolecular Studies. *The Journal of Physical Chemistry Letters*, 10(24), 7878-7883.
https://doi.org/10.1021/acs.jpclett.9b03144

PAPER V: Joachim Kübel, Manoop Chenchiliyan, **Saik Ann Ooi**, Emil Gustavsson, Linnéa Isaksson, Valentyna Kuznetsova, Janne A. Ihalainen, Sebastian Westenhoff, Michał Maj. (2020).Transient IR spectroscopy identifies key interactions and unravels new intermediates in the photocycle of a bacterial phytochrome. *Physical Chemistry Chemical Physics*, 22(17), 9195-9203.
https://doi.org/10.1039/C9CP06995J

PAPER VI: Manoop Chenchiliyan, Joachim Kübel, **Saik Ann Ooi**, Giacomo Salvadori, Benedetta Mennucci, Sebastian Westenhoff, Michał Maj. (2023). Ground-state heterogeneity and vibrational energy redistribution in bacterial phytochrome observed with femtosecond 2D IR spectroscopy. *The Journal of Chemical Physics*, 158(8).
https://doi.org/10.1063/5.0135268

PAPER VII: Pankaj Bharmoria, **Saik Ann Ooi**, Andrea Cellini, Daniel Tietze, Michal Maj, Kasper Moth-Poulsen, Alesia A. Tietze. (2023). Protein cohabitation: long-term immunoglobulin G storage at room temperature. *Journal of Materials Chemistry B*, 11(24), 5400-5405.
https://doi.org/10.1039/D3TB00161J

Contribution report

PAPER I: I planned the experiments, analyzed the data, prepared the figures, and contributed to writing the manuscript.

PAPER II: I planned the experiments, synthesized and purified the peptides, prepared the grids for both negative stained EM and cryo-EM, collected and analyzed data, prepared the figures, and wrote the manuscript.

PAPER III: I was involved in the planning of the experiments, contributed to the discussion of the results and wrote sections of the manuscript.

Abbreviations

AFM	**A**tomic **F**orce **M**icroscopy
AMY	**AMY**lin receptors
AWI	**A**ir **W**ater **I**nterface
Boc	*tert*-**b**ut**o**xy**c**arbonyl
CD	**C**ircular **D**ichroism
CMC	**C**ritical **M**icelle **C**oncentration
Cryo-EM	**C**ryogenic-**E**lectron **M**icroscopy
CTF	**C**ontrast **T**ransfer **F**unction
CTR	**C**alci**t**onin **R**eceptor
DACRA	**D**ual **A**mylin **C**alcitonin **R**eceptor **A**gonist
DCM	**D**ichloro**m**ethane
DIC	*N,N′***Di**isopropyl**c**arbodiimide
DMF	**D**i**m**ethyl**f**ormamide
DMSO	**D**i**m**ethyl **s**ulf**o**xide
EM	**E**lectron **M**icroscope
Fmoc	9-**f**luorenyl**m**ethyl**o**xy-**c**arbonyl
FTIR	**F**ourier **T**ransformed **I**nfra**r**ed spectroscopy
GPCR	**G**-**P**rotein-**C**oupled **R**eceptor
GLP1	**G**lucagon-**L**ike **P**eptide-1
HBTU	**H**exafluorophosphate **B**enzotriazole **T**etramethyl **U**ronium
HEPES	4-(2-**h**ydroxy**e**thyl)-1-**p**iperazine**e**thane**s**ulfonic acid
hIAPP	**H**uman **I**slet **A**myloid **P**oly**p**eptide
HFIP	**H**exa**f**luoro**i**so**p**ropanol
HPLC	**H**igh **P**erformance **L**iquid **C**hromatography
IR	**I**nfra**r**ed Spectroscopy
LCMS	**L**iquid **C**hromatography-**M**ass **S**pectrometry
MES	2-(N-**m**orpholino)**e**thane**s**ulfonic acid
MOPS	3-**m**orph**o**lino**p**ropane-1-**s**ulfonic acid
MicroED	**Micro**crystal **E**lectron **D**iffraction
MS	**M**ass **S**pectrometry
NMR	**N**uclear **M**agnetic **R**esonance
PBS	**P**hosphate **B**uffer **S**aline
RAMP	**R**eceptor **A**ctivity-**M**odifying **P**rotein
RELION	**RE**gularized **LI**kelihood **O**ptimisatio**N**
rIAPP	**R**at **I**slet **A**myloid **P**oly**p**eptide
SDS	**S**odium **D**odecyl **S**ulfate

SPA	**S**ingle **P**article **A**nalysis
SPPS	**S**olid **P**hase **P**eptides **S**ynthesis
STEM	**S**canning **T**ransmission **E**lectron **M**icroscopy
Tris	**Tris**(hydroxymethyl)aminomethane
***t*Bu**	***t*-bu**tyl
TEM	**T**ransmission **E**lectron **M**icroscopy
TFA	**Trif**luoro **A**cetic acid
TIS	**T**ri**i**sopropyl**s**ilane
ThT	**Th**ioflavin **T**
WT	**W**ild **T**ype
2D	**T**wo **D**imensional
2DIR	**T**wo **D**imensional **I**nfra**r**ed spectroscopy
3D	**T**hree **D**imensional

Contents

Chapter 1

Introduction

Proteins are one of the building blocks of life. They provide structural support for cells and regulate gene expression, the immune system, and biochemical processes in the body. Proteins are macromolecules that are made up of molecular building blocks known as amino acids. Amino acids are organic compounds consisting of an amino group, a carboxyl group, and a side chain. There are 20 naturally existing amino acids that differ in their chemical properties governed by the nature of their side chain [1]. Smaller proteins with less than 50 amino acids are known as peptides. A well-known example of a peptide is insulin, an essential hormone in the body, which controls the blood sugar levels and glucose uptakes from the blood.

Proteins fold into a three-dimensional (3D) structure based on their sequence of amino acids. The protein structure can be defined with four levels: primary, secondary, tertiary, and quaternary structures [2]. The primary structure is the sequence of the polypeptide chain which consists of the amino acids connected through peptide bonds. The carboxyl group can form hydrogen bonds with neighboring amino acids, leading to the folding of the protein's secondary structure. This secondary structure can consist of motifs such as α helices or β-sheets. The tertiary structure of the proteins is formed when the side chains of the amino acids interact through hydrophobic interaction, disulfide bond, or non-covalent bond interaction. In some proteins an additional structure level, the quaternary structure is observed, where it describes the arrangement of several subunits. An example of a protein with a quaternary structure is insulin which consists of two polypeptide chains. The DNA of the gene codes the sequence of amino acids. When mutations happen, they change the DNA of the gene, which then changes the amino acid sequence which can affect the functionality of the protein.

1.1 Protein misfolding

The mechanism of how proteins fold into the 3D structure from the primary structure is a complex process. However, the protein folding process is certainly guided by the amino acid sequence, as the folding does not occur randomly [3]. Several molecular interactions such as hydrophobic interactions, disulfide bridges, and side-chain interactions stabilize the protein in its native state. Some proteins are folded while they are being synthesized by the ribosomes, whereas some proteins are folded in the cytoplasm and other specific compartments of cells [4].

Theoretically, the folding of proteins can be described with a free-energy landscape for a specific amino acid sequence, where the x-axis is the conformation of structures and the y-axis is the energy. The unfolded conformations have high free energy, and the native conformation that is thermodynamically stable usually has the lowest free energy in the free-energy landscape; thus forming a funnel-like shape where the protein will fold from high to low energy through the funnel as shown in Figure 1.1. The presence of molecular chaperones helps the protein fold to its native structure when the folding process can be complicated [5]. However, even with the help of a chaperone, the protein might follow a wrong folding pathway and fall into a different local minimum. In this case, the protein is folded incorrectly, known as the misfolded protein. Instead of following the funnel-like trajectory as a correct folding occurs, the misfolded proteins create a rugged energy landscape with different lowest minimum energy [3]. In some cases, the same protein can be folded incorrectly into several local minima, leading to proteins folded with different structures, known as polymorphism.

The correct folding of proteins is essential for the proteins to function biologically, whereas misfolded proteins are hence either not functional or may have a harmful function. Therefore the misfolded proteins are usually degraded with ubiquitin-proteasome system and autophagy [6]. However, some misfolding proteins could avoid the degradation and instead accumulate, leading to malfunction of biological processes in the body and diseases.

1.2 Amyloids

Amyloids are misfolded protein aggregates that form elongated fibrils with cross-β architecture. The presence of amyloid fibrils can be detected by using specific dyes: Congo Red for the tissue sections [7], or Thioflavin-T(ThT) when being detected *in vitro* [8]. When the fibrils are visualized with atomic force microscopy or electron microscopy, they show a similar appearance:

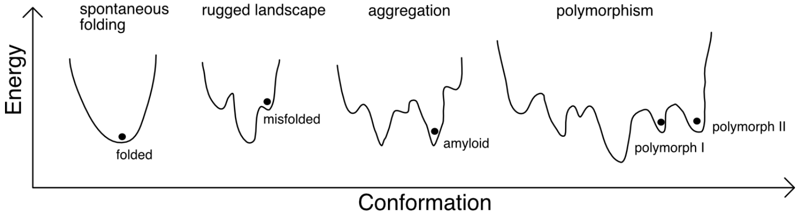

Figure 1.1: The free-energy landscape of protein folding. A correctly folded protein should have a funnel-like landscape as shown in spontaneous folding, whereas misfolded proteins tend to have a rugged-like funnel.

a thin and long rod-like structure that can be bundled together. Furthermore, X-ray fibril diffraction shows a distinctive diffraction pattern, known as the cross-β pattern, which originates from the β-sheets in the fibrils [9]. Since amyloids are stabilized by the interaction between main chains, such as hydrogen bonding, the β-sheets structures of all amyloid proteins look similar even though they originate from completely different amino acid sequences.

Aggregation of amyloids occurs through the nucleation mechanism, which shows a characteristic sigmoidal curve as presented in Figure 1.2. Initially, the peptide is in the monomeric state, from which toxic oligomeric species form throughout the so-called lag phase period [10]. Increasing concentration of oligomeric species ultimately results in the formation of a nucleus that accelerates the aggregation process towards the final product, i.e. the β-sheet rich amyloid fibrils. It is known that amyloid fibrils tend to form into different variations of fibrils, known as polymorphism [11].

The deposition of amyloid in tissues interferes with the normal functioning of organs. Such a condition is also known as amyloidosis and has been linked to many human diseases. There are two types of amyloidosis, localized and systemic amyloidosis. When the amyloid is only deposited at the site of production, affecting only one organ, it is known as localized amyloidosis, which is for example observed in patients with Alzheimer's disease, Parkinson's disease, prion diseases, and type 2 Diabetes. When the amyloid is a circulating protein and involves multiple organs, it is known as systemic amyloidosis, such as transthyretin amyloidosis (ATTR), immunoglobulin light chain amyloidosis (AL), and dialysis-related amyloidosis [12].

1.3 Human islet amyloid polypeptide

In the islets of type 2 diabetes patients, insulin-resistant obese patients, and patients with impaired glucose tolerance, healthy β-cells were found to be

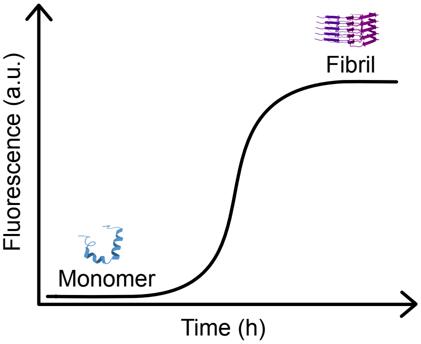

Figure 1.2: The schematic representation of the aggregation kinetics of amyloid which starts from the lag phase consisting of monomers and eventually forming fibrils in the plateau phase. Monomer PDB: 2L86, fibril PDB: 8QVR

replaced by highly concentrated amyloid plaques. The amyloid was later identified as human islet amyloid polypeptide (hIAPP or amylin) [13, 14]. The presence of amyloid deposits is not detected in healthy patients hence the aggregation of hIAPP has been linked to the loss of β cells (Figure 1.3) [15]. In addition to that, the production of insulin will be impaired as well since insulin and hIAPP are co-secrete in β-cells. The reduced production of those hormones will affect the regulation of glucose. Thus, when the number of β cells is reduced and their function impaired, insulin resistance and type 2 diabetes develop more rapidly [16].

The hIAPP is a 37 amino acids long peptide, with an amidated C-terminus and a disulfide bridge between cysteines located at positions 2 and 7. From the physiological perspective, hIAPP is a hormone peptide that is stored and co-secreted along with insulin in the β cells of the pancreatic islets. The function of hIAPP is to delay gastric emptying and inhibit glucagon secretion which leads to the reduction of blood glucose levels in the blood and also the body weight [17].

Amylin receptors, which are found in the central nervous system, mediate the function of hIAPP. There are three types of amylin receptors ($AMY_{1\text{-}3}$), which consist of a heterodimerized structure of the calcitonin receptor (CTR) associated with one of the receptor activity-modifying proteins (RAMPs) [18]. CTR is a seven-transmembrane G-protein-coupled receptor (GPCR) located on the cell membrane. In contrast, RAMPs are a single transmembrane spanning domain with an extracellular N-terminal domain and a short intracellular C-terminal domain [19]. CTR has a lower affinity with hIAPP when it interacts with hIAPP on its own, however, with the association of one of the RAMPs, the affinity towards hIAPP increased [20].

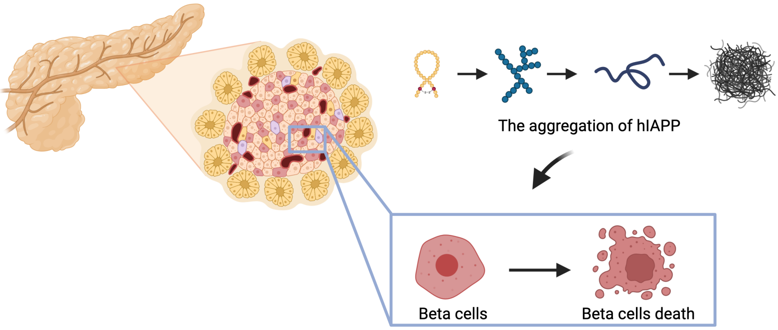

Figure 1.3: When hIAPP aggregates from monomer to fibrils in the β cells, the number of healthy β cells is also found to be reduced, indicating that the presence of amyloid destroyed the β cells. Created with Biorender.

1.4 Structural characterization of hIAPP

Different techniques can be used to determine the secondary and tertiary structure of proteins. Circular dichroism (CD) and Fourier transform infrared spectroscopy (FTIR) are commonly used to study the overall secondary structure of the proteins such as α-helical or β-sheets during the aggregation kinetics [21]. Atomic force microscopy (AFM) [22], transmission electron microscopy (TEM) [23], and scanning transmission electron microscopy (STEM) [24] are used as a more direct imaging technique to visualize the morphology of the fibrils after aggregation. However, the atomic details of the aggregation mechanism cannot be elucidated by those techniques.

Despite much effort, the structure determination of hIAPP remains challenging due to the nature of the amyloid. The heterogeneity and insolubility of amyloid make it difficult to study the structure of fibrils by using solution nuclear magnetic resonance (NMR) spectroscopy. However, the emergence of solid-state NMR enables the study of amyloid structure by using lyophilized sample instead of a solution, thereby avoiding the solubility limitation. In the beginning, most of the studies were conducted with truncated versions of hIAPP as a model to study. For example, a truncated version of hIAPP with residue 20 to 29, was studied with solid-state NMR [25–27], and solution NMR in the presence of sodium dodecyl sulfate (SDS) micelles [28]. At that time, full-length hIAPP was challenging to synthesize due to the hydrophobicity and several β-branched amino acids in the sequence. When the synthesis of full-length hIAPP became readily accessible by incorporating pseudoprolines and microwave-assisted synthesis later [29,30], more structural and aggregation studies have been conducted with full-length hIAPP [31,32]. Later on, solution NMR was used to study the structure of hIAPP in a physiological environment in the lipid membrane by using SDS to form the micelle [33], and even the monomeric hIAPP in solution [34].

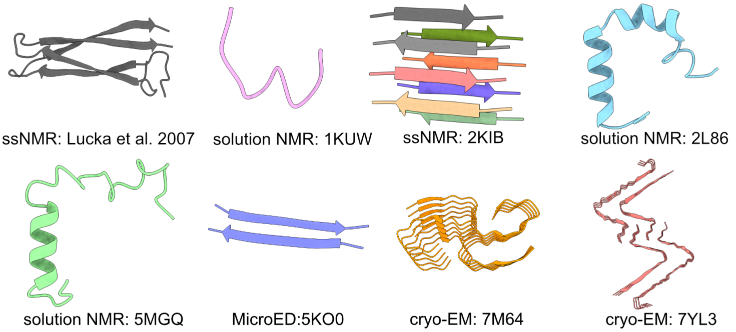
ssNMR: Lucka et al. 2007
solution NMR: 1KUW
ssNMR: 2KIB
solution NMR: 2L86
solution NMR: 5MGQ
MicroED:5KO0
cryo-EM: 7M64
cryo-EM: 7YL3

Figure 1.4: 3D structures of hIAPP that have been solved previously with different techniques: ssNMR, solution NMR, MicroED, and cryo-EM.

X-ray crystallography which is commonly used to study the structure of proteins, is not feasible for hIAPP due to the challenge in crystallizing amyloids. However, microcrystal electron diffraction (MicroED), the combination of x-ray diffraction and electron microscope, has been used to solve the structures of truncated hIAPP as they were capable of forming crystals [35]. Figure 1.4 illustrates some structures that have been solved using different techniques.

In recent years, the rapid development of software, hardware, and cryo-electron microscope (cryo-EM) created the possibility of studying amyloid fibrils in native conditions and solving the structures at high resolution. Several fibril structures of hIAPP wildtype (WT), patient samples seeded with *in vitro* WT, and mutant fibrils (S20G) have been published at resolutions between 3 to 4 Å. [36–40]. Cryo-EM uniquely allows for the individual identification and separation of amyloid fibril polymorphs, which is not the case for spectroscopic techniques, such as NMR.

The focus on the secondary structures of hIAPP has thus shifted with these advancements, offering new insights into how hIAPP aggregates at the atomic level. Since the accumulation of hIAPP amyloid contributes to the death of the β cells and aggravates type 2 diabetes, understanding the aggregation mechanism and structures of fibrils provides perspective on how to slow down or even prevent the aggregation. Furthermore, atomic analysis of the hIAPP structure provides an idea of how hIAPP interacts with the CTR-RAMPs. This interaction is key in the development of hIAPP-based homolog compounds, potentially leading to innovative therapeutic approaches.

1.5 IAPP-based mimetics as potential therapeutic agents

Building on these insights, the development of hIAPP-based mimetics emerges as a promising avenue for type 2 diabetes treatment. Since hIAPP is a human hormone, it should have a lower immunogenicity which will not incur unwanted immune response when administered, hence it may be used as a promising drug to support existing therapies for type 2 diabetes [41]. Moreover, hIAPP's role as a satiety agent offers added benefits in weight management for diabetic patients [42]. However, the inherent propensity of hIAPP prohibits its use and poses a challenge in formulating a soluble solution to be used as a therapeutic. Rat IAPP (rIAPP), on the other hand, does not aggregate in nature despite only six amino acid differences in its sequence [43].

Pramlintide is a drug designed based on the inspiration of three prolines from rIAPP, which has been approved and is being used in complement with insulin for type 1 and 2 diabetes treatment [44]. Even though Pramlintide is soluble, it has to be formulated at pH 4 to prevent the breakdown of the drug from deamination and backbone hydrolysis [45]. On the other hand, insulin is formulated at pH 7.8 [46]. Due to the pH differences, two separate injections of pramlintide and insulin are required, which can be inconvenient for the patients. Furthermore, pramlintide requires frequent administration due to its short half-life, which is about 20 to 50 minutes [46]. An ongoing clinical trial where co-formulation of both Pramlintide and insulin in the same injection is performed for patients with type 1 diabetes [47,48].

In addition, there is another ongoing clinical trial of an hIAPP-analog drug, Cagrilintide which is a dual amylin and calcitonin receptor agonist (DACRA) [49,50], provides a promising result for the treatment of type 2 diabetes and weight loss. It interacts with both receptors, CTR and ($AMY_{1\text{-}3}$). However, this drug is intended to be formulated at low pH with once-a-week injection and can be used together with glucagon-like peptide (GLP1) instead of insulin.

In short, those clinical trials indicate that a drug designed closely based on the hIAPP sequence is a potential drug as it has the highest effect on weight loss in comparison to other drugs. For type 2 diabetes patients, maintaining a healthy weight can reduce insulin resistance and better control of glucose levels in the body, which reduces the risk of complications to other organs and cardiovascular disease.

1.6 Scope of Thesis

Type 2 diabetes is an epidemic that affects millions of people in the world, yet the exact mechanism of how this disease formed is still unclear. Insulin resistance and obesity used to be the root of the disease, but recently the loss of β-cells has been discussed as a potential cause that leads to type 2 diabetes [51]. It has been known that the aggregation of hIAPP amyloid leads to the death of β-cells. Thus, understanding the mechanism of hIAPP aggregation from a monomer peptide to amyloid is essential to designing an efficient drug treatment for type 2 diabetes.

This thesis focused on understanding the mechanism of hIAPP aggregation through different approaches. The structures of hIAPP solved in cryo-EM were aggregated in buffers either at pH that is not physiological conditions or with an additional tag. Since the accumulates of hIAPP are mostly found outside the cell at pH 7.4 [52], solving the structure of hIAPP fibrils at physiological conditions would be of interest. Therefore, the optimization of cryo-EM grid preparation was carried out, enabling the very first determination of the *in vitro* structure of hIAPP fibrils at physiological pH. The results have been summarized in **Chapter 3**.

Pramlintide has been designed based on the proline mutations of rIAPP and provided promising results as a drug to treat type 2 diabetes in complement with insulin. However, due to the drug's properties, fewer patients have been prescribed this drug. Designing a drug similar to hIAPP would offer a huge advantage especially promoting weight loss in diabetic patients. Thanks to the advancement of cryo-EM, more 3D structures of hIAPP fibril have been solved, which offers insight on how the structures are stabilized. Proline is known as a β-sheet breaker which could be the reason that Pramlintide does not aggregate. As the amyloidogenic core has always been emphasized in hIAPP studies, the prolines from Pramlintide and rIAPP have been mutated individually on the hIAPP core to evaluate the effect of proline on the formation of fibril. Through cryo-EM, the study has shown that each mutant formed diverse polymorphisms that are not found in published structures, which has been included in **Chapter 4**. The information is useful for suggestions on the potential mutation to create a non-amyloidogenic hIAPP as a potential therapeutic target.

Another promising approach to reducing the death of β-cells is through inhibition of the aggregation of hIAPP. Many small molecules have been shown to have an inhibitory effect on hIAPP. With a similar sequence, rIAPP has been shown to inhibit the aggregation of hIAPP as well through an undiscovered mechanism. On the other hand, rIAPP is also involved in the fibril formation of hIAPP, creating hybrid fibrils. Hence, **Chapter 5** focuses on the investigation of the concentration-dependent inhibitory effects of rIAPP on hIAPP to elucidate the potential mechanism. In addition, different buffer conditions have been tested to study the effect of the environment affecting fibril polymorphism, which is investigated by cryo-EM. The ThT kinetics and 2D class averages have shown that the aggregation has been affected to a great extent by the concentration of rIAPP and buffer conditions.

Chapter 2 describes the methods used throughout the thesis, including peptide synthesis and purification, the aggregation kinetics of the fibrils *in vitro*, and an overview of cryo-EM. Lastly, the summary of the work discussed in this thesis and future remarks are included in **Chapter 6**.

Chapter 2

Method

2.1 Peptide synthesis and purification

Peptides are often produced through chemical synthesis. One of the most commonly used methods is solid phase peptide synthesis (SPPS) [53], where the amino acids are coupled step-wise to a solid support, known as resins. Resins are beaded polystyrene with insoluble linkers in common solvents that can produce different C-terminal groups upon cleavage. For example, PAL-PEG-PS or Tentagel R RAM resin can be used to produce the C-terminal amide group.

The first amino acid from the C-terminus is coupled to the resin as the synthesis is performed from the C-terminus to the N-terminus. The reactive N-terminal and side chains of amino acids should be protected to prevent polymerization and reduce undesirable side reactions. There are two common protecting groups for N-terminal amine, *tert*-butoxycarbonyl (Boc) or 9-fluorenylmethyloxy-carbonyl (Fmoc) [54]. Fmoc is more favorable over Boc, as Boc requires hydrogen fluoride in the final cleavage step, whereas Fmoc requires a mild base, such as piperidine. Furthermore, Fmoc is usually used in combination with *t*-butyl (*t*Bu) based side chain protecting groups, where the protecting group is removed with trifluoroacetic acid (TFA).

Peptides are prone to aggregate which can cause problems during the synthesis. To prevent this, pseudoproline dipeptides can be used to improve peptide synthesis [55]. They consist of two amino acids, such as Leu and Ser that have been reversibly protected in a proline-like structure, and will revert to normal amino acids of Leu and Ser during the deprotection step as TFA will break the oxazolidine. Since hIAPP is prone to aggregate, two pseudoprolines have been used to improve the synthesis. Fmoc-Ala-Thr(Psi(Me,Me)pro)-OH that is used at positions 7, 8 and Fmoc-Leu-Ser(Psi(Me,Me)pro)-OH at positions 27, 28 [30].

Nowadays, a synthesizer instrument is usually used for SPPS where all the steps are performed automatically and controlled by software. Before the start of the synthesis, the resin is swelled with an organic solvent, typically dichloromethane (DCM) or dimethylformamide (DMF), for at least half an hour to have an efficient coupling of amino acids. The Fmoc protecting group of the linker of the resin is deprotected with 20% piperidine in DMF and the resin will subsequently be washed with DMF. After that, the C-terminal carboxylic acid of the next amino acids will be activated with a coupling reagent such as *N,N′*-diisopropylcarbodiimide (DIC), or hexafluorophosphate benzotriazole tetramethyl uronium (HBTU) for coupling to the resin. This step can be repeated to improve the coupling of the amino acids, which is known as double coupling. A DMF wash will then remove the excess reagent. The N-terminal protecting group of the newly coupled amino acid will be deprotected with piperidine to allow the coupling of the next amino acids. These steps will be repeated until all the amino acids in the sequence have been coupled. A typical SPPS flowchart is shown in figure 2.1.

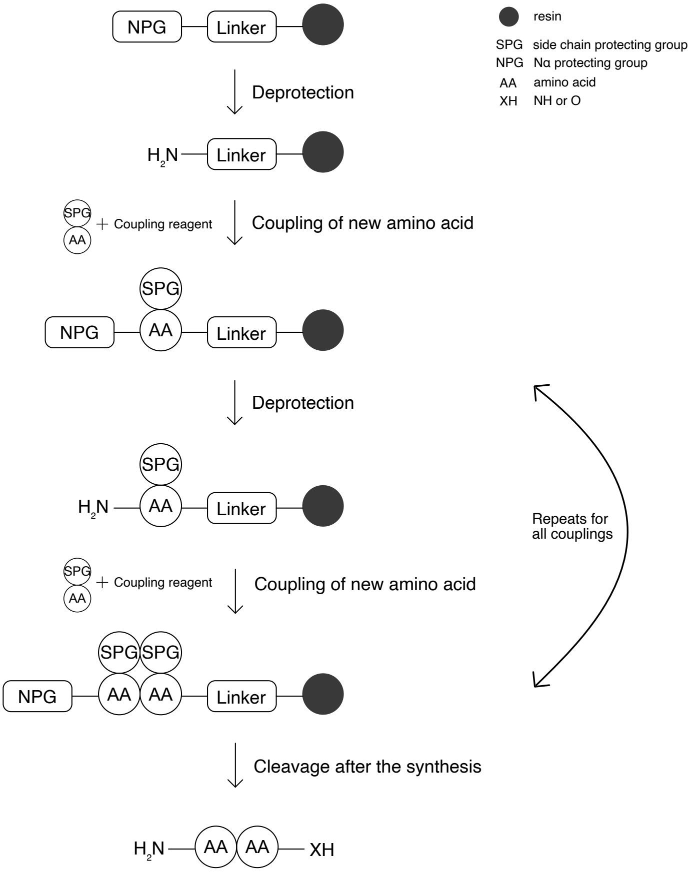

Figure 2.1: The flowchart of a general SPPS protocol. The resin is deprotected, followed by the coupling of a new amino acid and deprotection of the new amino acid. The steps are repeated until all amino acids are coupled.

Once the synthesis has been completed, a cleavage cocktail is incubated with the resin for 2-3 hours to remove the peptide from the resin. There are different formulations of cleavage cocktails depending on the side chain protecting groups, as some chemicals will be added to scavenge the side chain protecting groups to prevent undesired reactions to the peptide. The cleavage cocktail with TFA, triisopropylsilane (TIS), and water has been used for hIAPP synthesis. Excess cleavage cocktail will be evaporated using nitrogen gas, ice-cold ethyl acetate is then added to precipitate the crude peptide. To get rid of the leftover cleavage cocktail, the crude peptide is dissolved in water and then lyophilized overnight.

To form the disulfide bridge between Cys2 and Cys7 of hIAPP, dimethyl sulfoxide (DMSO) is incubated with the lyophilized peptide for 24 hours [56]. After the formation of the covalent bond, the peptide is purified using high-performance liquid chromatography (HPLC). Reverse phase HPLC is used where the stationary phase is non-polar and the mobile phase is polar. The stationary phase consists of silica, here a C18 column is used which is octyldecylsilane that contains 18 carbons bound to the silica. Having more carbons provides a bigger surface area where the sample will take a longer time to interact and elutes slower, which provides better separation. A more polar sample elutes faster in reverse-phase HPLC since the polarity of the mobile phase dictates how fast a sample elutes in the purification. The mobile phase consists of two different buffers. Depending on the sample, the buffers can be kept at a constant ratio (isocratic); or the ratio can be gradually changed throughout purification (gradient). Gradient elution is normally used for protein and peptide purification as it separates complexes with different molecular weights and hydrophobicity more efficiently in comparison to isocratic elution. For hIAPP, buffer A consisted of 100% H_2O with 0.045% HCl and buffer B consisted of 80% acetonitrile with 0.045% HCl. A typical purification method for hIAPP usually starts with a high percentage of buffer A and ends with a high percentage of buffer B, where hIAPP usually elutes around 45% B.

In order to have hIAPP in the monomeric state, the purified peptides are dissolved in 100% hexafluoroisopropanol (HFIP) for several hours to monomerize the peptides. The concentration of the peptides is measured using absorbance at 280 nm with an extinction coefficient of 1490 $M^{-1}cm^{-1}$. The peptides are then aliquoted based on the concentration required. The HFIP is removed by lyophilizing overnight and the peptides are stored at -20°C until use.

2.2 Kinetics of amyloid formation

Molecular probes are commonly used to characterize the mechanism of aggregation and to detect the presence of amyloids in samples, as they undergo changes in their spectroscopic properties upon binding to fibrils. For instance, Congo red exhibits a pink color when it interacts with amyloid tissues, and under polarized light microscopy, it displays green birefringence [7].

For studying fibril formation *in vitro*, Congo red is considered less suitable due to its lower sensitivity compared to other molecular probes. Additionally, Congo red might interfere with the aggregation kinetics [57]. Instead, ThT is typically used for kinetic studies *in vitro* (Figure 2.2). When ThT binds to the β sheet structure, the C-C bond connecting the benzothiazole and aniline rings becomes immobilized in its fluorescent state [8]. Therefore, ThT is usually added together with the monomeric peptide to monitor fibril formation *in vitro*. ThT fluorescence can be measured using a plate reader, with the excitation wavelength set at 440 nm and the emission wavelength at 480 nm. The aggregation kinetics usually display a sigmoidal curve where there is no signal during the lag phase since ThT only binds to fibrils and does not fluoresce during the monomeric stage. As the peptides begin to aggregate and form fibrils, the signal increases exponentially and eventually reaches a plateau, indicating that all monomeric peptides have aggregated, as shown in Figure 1.2. Generally, ThT concentration is fixed at 20 µM to minimize the interference with the process of fibril formation.

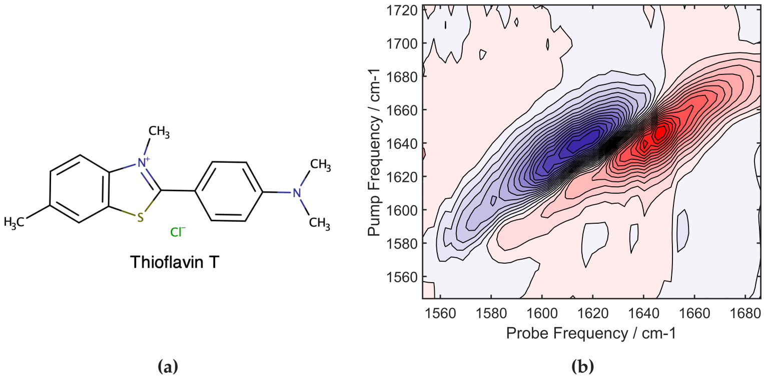

(a) **(b)**

Figure 2.2: a) The chemical structure of ThT for studying the aggregation kinetics of hIAPP *in vitro*. b) An example of the 2DIR spectrum collected from hIAPP, where the pump frequency at around 1640 cm^{-1} indicates that the hIAPP consists of β-sheets, which is the fibrils state.

In addition to the use of molecular probes like ThT, infrared (IR) spectroscopy is another method that can be used to investigate the secondary structure of proteins. The absorption of IR light excites the vibrational transitions in molecules whose frequency and lineshape depend on the intramolecular and intermolecular interactions. In the context of proteins, these vibrational transitions arise from the protein backbone and amino acid side chains. The major bands in the IR spectrum for proteins are amide I: which originates from the C=O stretching, and amide II: which originates from N-H bending. The frequencies that contribute to amide I generally come from different secondary structures and hydrogen bonding interactions, such as α-helix (1655 cm^{-1}), β-sheet (1630 cm^{-1}) and β turns (1680 cm^{-1}) [58].

While both ThT kinetics and FTIR provide valuable data on the overall secondary structure of proteins, pinpointing the specific amino acids contributing to the signal remains challenging. In contrast, the application of two-dimensional infrared spectroscopy (2DIR), particularly when combined with $^{13}C^{18}O$ isotope labeling, offers enhanced sensitivity to minor changes in the secondary structure at the labeled residue [59]. Additionally, time-resolved 2DIR can be used to elucidate the picosecond solvation dynamics of the species under investigation which offers additional information on the aggregation process [60–62]. An illustrative example of a 2DIR spectrum of hIAPP is presented in Figure 2.2.

2.3 Electron microscopy

Microscopes, with their ability to enlarge small objects, provide the necessary magnification for detailed and in-depth investigations of a variety of structures. An example of a microscope is a light microscope where an object is placed over a glass slide, and the image of the object is magnified by glass lenses and illuminated by a light source. The maximum resolution of the images achievable is usually half of the wavelength of the light source. Visible light has a wavelength between 380 and 700 nm and thus the highest resolution that can be achieved with a light microscope is roughly 200 nm.

Electron microscopes (EM) allow for better resolution of the images as compared to light microscopes by using electron beams which have a shorter wavelength than visible light. The electron beam is generated by accelerating electrons across a potential difference of up to several hundred kilovolts. The electron microscope has to be operated in vacuum conditions to prevent electron beams from losing energy by interacting with other molecules usually present in the air while traveling toward the sample. Furthermore, instead of glass lenses, electromagnetic lenses are controlled by electric current to align the beam and magnify the resulting image in EM. The sample has to be thin enough for the electron beams to pass through. The electrons will then carry information about the sample further, caused by the interaction between the electrons and atoms in the sample, which can then be recorded with electron imaging devices.

There are two types of EM: transmission electron microscopy (TEM) and scanning electron microscopy (SEM). TEM is typically used to study the internal structures of cells, such as protein configurations, while SEM is commonly employed to examine the surfaces of cells or organisms. In this thesis, the research focuses on TEM, utilizing both negative staining and cryo-electron microscopy techniques.

2.3.1 Negative stain

Negative stain TEM is typically performed first to assess the quality of the sample following its purification to high purity. This method is relatively inexpensive and quick compared to the preparation of cryo-EM samples and is carried out at room temperature. Biological samples, mostly composed of light elements, do not provide sufficient contrast under the microscope. To address this, an additional heavy metal, such as uranyl salts, is used to enhance electron scattering [63]. These heavy metals do not stain the sample directly; rather, they stain the area around the sample, creating what is known as negative contrast.

For visualization in EM, the biological sample must be placed onto a grid, which is a small round mesh support made from materials like copper or gold and covered with a film. To prepare for use, the grids are glow-discharged to modify their surface properties from hydrophobic to hydrophilic, ensuring a uniform distribution of the sample on the grid. A small volume of the sample, approximately 5 µL, is then applied to the grid. After a brief incubation period, any excess sample is removed with filter paper, and a heavy metal solution, typically uranyl formate, is applied to the grid and allowed to dry. The grid is ready for use in the TEM once it has completely dried

2.3.2 Cryo-EM

The primary distinction between negative stain TEM and cryo-EM lies in the preparation of cryo-EM grids, which are made under cryogenic conditions and without the use of heavy metals (Figure 2.3). This approach allows proteins to be studied in an environment that more closely resembles their native state compared to other techniques. Moreover, structures resolved using cryo-EM typically exhibit higher resolution than those obtained with negative stain TEM, which usually have a resolution of around 10 Å. The highest resolution structure solved by cryo-EM to date is apoferritin, with a final resolution of 1.25 Å [64].

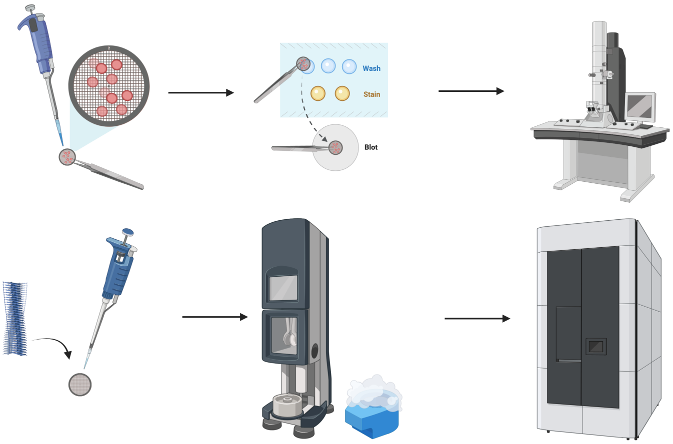

Figure 2.3: The differences between negative stain EM and cryo-EM from grid preparation to visualization. Created with Biorender.

Once the protein of interest has been preliminary evaluated with negative stain EM and deemed worthwhile to continue the work in cryo-EM, the protein will be frozen swiftly using liquid ethane to preserve the protein in the solution environment. Once the grids are frozen, they must be kept in liquid nitrogen until being visualized in the microscope. If not, thicker ice layers might form on the grid and reduce the quality or even the possibility of data collection.

Several parameters are crucial to achieving fruitful data collection: starting from the sample, the type of grids, the settings in the microscope, and even the strategy to collect the data. The sample should have an optimum concentration that provides an even distribution of particles on the grid and does not overlap with each other as those particles will not be useful in image processing. Depending on the sample, the size of the grid hole can affect the formation of ice thickness level since the sample will be frozen into a thin layer of ice. One of the commonly used grids is Quantifoil R 2/2, where the grid holes are 2 µm and the distance between the grid holes is 2 µm. Sometimes a bigger grid hole can be used for fibrils since fibrils tend to be long and a bigger grid hole can hold more fibrils instead of ending up on the carbon surface.

There are several parameters within the microscope that can affect data collection as well as the final resolution of the images. The Nyquist limit generally describes the maximum image resolution achievable, which is twice the pixel size of the detector [65]. For instance, if the pixel size used is 1 Å, the maximum theoretical resolution would be 2 Å. However, this is not always attainable in practice due to other influencing factors within the microscope. Pixel size refers to the physical distance between each pixel, which varies based on the microscope's magnification. Higher magnification results in a smaller pixel size, enabling the resolution of structures at higher detail. However, this approach can be computationally expensive.

In cryo-EM, the objective lens of the microscope is commonly set to slightly underfocus to enhance phase contrast during imaging as biological samples affect the phase more than the amplitude [66]. When the imaging is acquired at the exact focus, the contrast of the sample is so weak that the detail of the sample cannot be solved. A higher defocus value provides a stronger contrast but also is limited to the range of high-resolution information, whereas a lower defocus value has a wider range of high-resolution information but with a weaker contrast. Thus, instead of setting a single defocus value, a range of defocus values have been used to acquire the images to include all information of the sample.

Having a high electron dose could provide high-contrast images, however, the sample will also be destroyed due to radiation damage; on the other hand, having a too-low electron dose might provide too weak of a contrast. Furthermore, electron beams also induced movement of the sample during the collection. Thus, instead of imaging a single micrograph at a higher electron dose, multiple frames of images are collected at a lower dose and combined into movies, where they are averaged to improve the contrast.

Since the protein structure is usually taken on a 2D view and low contrast, the micrographs need to be analyzed using software that allows combining multiple 2D views to reconstruct them into a 3D structure.

2.3.3 Grid optimization

The grids in cryo-EM are prepared through vitrification. The sample is added to a grid where the excess solution of the sample is then blotted away and plunged frozen immediately in liquid ethane. This creates a thin film of ice with the sample embedded in it. Liquid ethane is used as it has a higher heat capacity than liquid nitrogen. When the sample is dipped into liquid ethane, it does not absorb the heat from the sample and boils off some part of it, which might form crystalline ice on the grid as this is what would happen with liquid nitrogen. However, liquid ethane is cooled by liquid nitrogen during the vitrification to ensure that liquid ethane is in the liquid state.

To have a reproducible grid preparation, this step can be conducted with commercial instruments, such as Vitrobot [67], which is carried out in a closed environment. Various parameters can be adjusted during the grid freezing, such as blot force, blotting time, humidity, and temperature.

However, even with the closed environment and controlled parameters, the grids are not always reproducible, such as the ice thickness and amount of samples in the grid. Especially for fibrils where the chunk of fibrils might be removed during the blotting step.

The grids should have a good distribution of analytes over the grid holes and a thin layer of ice for efficient data collection. Various factors can be changed during the optimization of the grid which are crucial to improving the grids, including the buffers, pH, additives, grid types, and freezing conditions.

2.3.4 Helical reconstruction

In cryo-EM data analysis, there are primarily two approaches: single particle analysis (SPA) and helical reconstruction, with cryo-electron tomography analysis being outside the scope of this thesis. SPA is employed for reconstructing protein structures, while helical reconstruction is utilized for analyzing fibrils and filaments [68,69]. The image processing steps are similar for both. For SPA, multiple orientations of the protein are needed for the 3D reconstruction. However, the helical parameters as shown in Figure 2.4, such as the rise and the twist, are required for the 3D reconstruction of fibrils [70]. The rise is the distance between each β-sheet layer in fibrils, and the twist is the rotation of each layer. The crossover distance can be calculated from the rise and twist with the equation below [70]:

$$twist = \frac{4.75\text{Å} \times 180^\circ}{crossover}$$

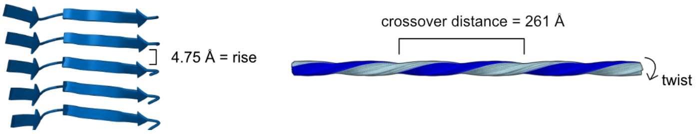

Figure 2.4: The helical parameters that are needed in a helical reconstruction. The rise is typically found at 4.75 Å and the crossover distance can be calculated from the twist.

The typical workflow for image processing starts with importing the micrographs and pre-processing them with motion correction and contrast transfer function (CTF) estimation. The beam-induced motion of the samples is corrected by aligning the frames on a specific feature to have a better resolution final image. In addition, since the movies are collected at a lower electron dose, they are improved with a dose weighting algorithm where the frames with good resolution information are assigned with higher weight and frames with more radiation-damaged information are assigned with a lower weight. The frames are then aligned and averaged based on the weight assigned to a single image which contains an improved quality final image [71,72].

The motion-corrected micrographs will be then used to estimate the CTF [73]. Various terms are included in the CTF, such as the electron wavelength, spherical aberration from the microscope, and the defocus of the images. Since the wavelength and spherical aberration are constant in the same dataset, therefore the defocus affects the CTF mostly. The contrast variations caused by the defocus will be corrected, thus providing the micrographs with reconstruction of high resolution information.

After the pre-processing, the particle of the sample will be picked either manually or through an automated algorithm. Nowadays there are numerous automated algorithms: template matching [74], blob picker [75], artificial intelligence, and machine learning-based approaches [76–78], and more. Some of the automated approaches require a model or template to serve as a reference for the picking. In general, it is common to start manually picking some of the micrographs to create a reference that can be used for the automated picking. Once the particles are picked, each particle will be extracted individually in a square box. Those extracted particles will be used to go through multiple alignments and averaging, such as 2D and 3D classification, to separate them into individual classes further. Generally, this step will be done iterative until one single class is chosen.

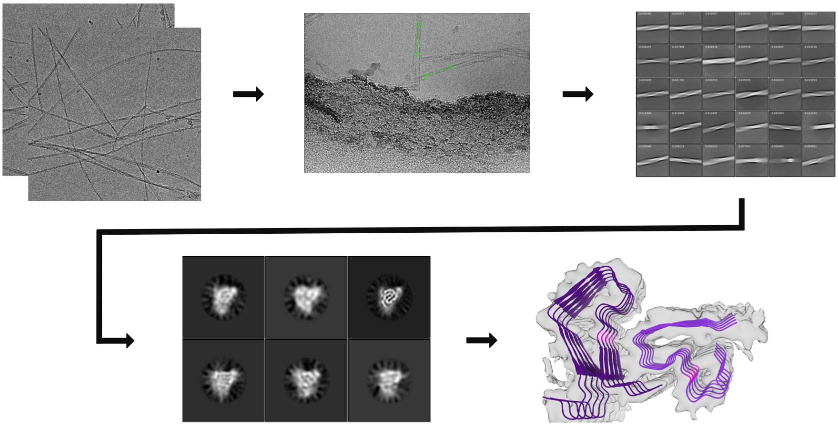

Figure 2.5: The flowchart of cryo-EM data analysis starts with importing movies into software, such as RELION. After the preprocessing of movies, particles are picked, where they are sorted with 2D or 3D classifications. Cleaned-up particles are then selected for high-resolution refinements, and finally, the protein model is built.

For helical reconstruction, instead of having one box for one fibril that will not fit well since the fibrils are long, multiple boxes will cover the whole fibril from start to end, thus each box will contain a part of the fibril. The 2D classification will align the particles that are coming from the same area into one class. During the 3D classification, the fibril is reconstructed into a 3D model with different classes of 2D classification that contain the information from start to end. A further alignment and averaging of particles will be performed during this step to obtain particles for one single structure. A high-resolution 3D map will be refined from the 'clean-up' particles. Sometimes, the refined map can be further post-processed to improve the resolution of the map. The workflow of cryo-EM analysis is illustrated in Figure 2.5.

Once a high-resolution cryo-EM map has been solved, it is now time to build the atomic model of the structure. If a homolog structure has been solved and deposited into the PDB, the PDB can be used as an initial model to fit the map and replace the amino acids that are different. However, if the structure is very different from the homolog structures, then the C-α backbone of the structure has to be built and fit each amino acid individually into the correct density [79]. Regardless, the atomic model will undergo refinement with some software to fit the map better and this step is usually carried out iterative until the model fits well [80]. Then the map and the atomic model will be assessed with validation tools [81]. Finally, the map and the atomic model will be uploaded to the PDB and relevant database.

Chapter 3

Grid optimization for cryo-EM of amyloid fibrils

Preparing cryo-EM grids for amyloid fibrils is an exceedingly challenging and unpredictable task in structural biology. Beyond producing protein samples, the substantial time investment in using the Vitrobot, coupled with the considerable costs of repeated sample screenings, makes the process particularly demanding for many research groups, especially those that rely on external cryo-electron microscopes. Currently, there are three Krios microscopes available in Sweden, which must meet the demands at a national level.

The challenges in cryo-EM of amyloid fibrils stem from frequent issues in grid preparation, including instability of vitreous ice films and poor particle distribution. These difficulties often require collecting an excessively high number of micrographs, sometimes over 10,000, to resolve a single high-resolution structure due to the diverse polymorphism inherent in amyloids.

This chapter presents a comprehensive compilation of extensive grid optimization efforts. It focuses on identifying optimal conditions for imaging fibril structures formed by WT hIAPP (paper I) and its proline mutants (paper II). The chapter discusses the optimal grid preparation protocols and provides a physicochemical rationale for their selection process.

3.1 The main challenges in grid optimization

Preparation of cryo-EM grids is a complex task that demands maintaining a delicate balance: the ice layer must be sufficiently thin while ensuring a uniform distribution of large number of particles. One of the primary complications during vitrification arises in the blotting steps, where fibrils are often unintentionally stripped away. This issue leads to varying amounts and uneven distribution of fibrils, despite careful grid preparation. Fibrils also tend to cluster together, forming spiderweb-like bundles on the grid. Moreover, during grid preparation particles frequently get adsorbed at the air-water interface (AWI). This interaction typically causes the particles to exhibit a preferred orientation on the grid.

However, well-separated fibrils are crucial for providing high-quality particles for the image processing of cryo-EM. For soluble and membrane proteins, additives, such as detergent, can be added to reduce the preferred orientation of particles [82]. In the case of fibrils, the addition of detergent may potentially improve the distribution of fibrils on the grid. However, using detergent as an additive can be challenging for amyloid fibrils and the concept remains largely unexplored in the context of amyloids. The reported concentrations of detergents required for single-particle cryo-EM are rather high, needing to be above the critical micelle concentration (CMC) to form the micelles, which leads to a lower contrast of samples with the background. Additionally, a high concentration of strong detergents might affect the secondary structure of amyloid fibrils or protofilaments as shown by spectroscopic studies [83, 84].

In addition to the distribution of fibrils, the ice quality is another big hurdle to overcome in fibril grid preparations. The instability of the ice layers cannot be guaranteed even when the grids are prepared under the same conditions. Since the ice quality cannot be judged before cryo-screening, the time and effort spent preparing the grids will be wasted. Thus, factors that could improve the ice thickness are also evaluated in this chapter.

Previous structures solved from hIAPP relied on the use of non-physiological pH buffers, N-terminal tags, and seeding [36–39]. Therefore, it is of interest to solve the structure from a physiological pH buffer. We have evaluated various buffer conditions to determine their influence on ice quality and fibril distribution. Additionally, various additives have been tested as well to compare their effects on grid improvement.

Grid optimization commonly begins with negative stain TEM, as preparing grids for cryo-EM is more time-consuming, costly, and requires careful handling. Negative staining provides an overview of the sample's behavior in various buffers and additives. Since this staining requires less than an hour for preparation, the grid can be almost immediately visualized using TEM. Once samples exhibit favorable behavior in negative stains, the same conditions can be applied to cryo-grid preparation. For optimizing grids for hIAPP-WT (discussed in paper I) and hIAPP-S29P (a mutant described in paper II), several factors were tested, including initial monomer concentration, the effects of salts, buffers, and additives. Grid optimization began with hIAPP-S29P, followed by hIAPP-WT.

3.2 Effects of initial monomer concentration

The aggregation of hIAPP-S29P was studied in tris(hydroxymethyl)aminomethane (Tris-HCl) at pH 7.4. Initially, a high concentration of 2 mg/mL (600 µM) was used for negative stain EM. However, this resulted in grids densely packed with overlapping fibrils, rendering them unsuitable for EM analysis. Aggregation under both shaking (400 RPM) and quiescent conditions failed to improve the results. Consequently, lower concentrations, specifically 100 µM and 300 µM, were tested to address the issue of clumping, as illustrated in Figure 3.1. However, even with these changes, the grids continued to display irregular fibril distribution, characterized by regions of both sparse and densely packed fibrils.

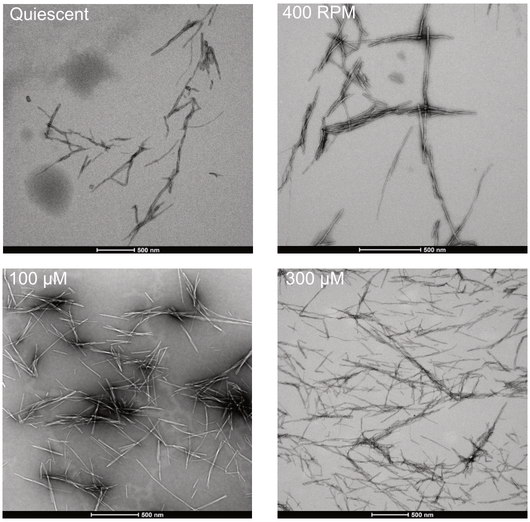

Figure 3.1: 600 µM of hIAPP-S29P in Tris-HCl pH 7.4 aggregated in quiescent condition or 400 RPM. The initial concentration of hIAPP-S29P monomer with 100 µM and 300 µM. No improvements were seen in growing the fibril in different conditions and starting the aggregation with lower initial monomer concentrations. Scale bar: 500 nm.

3.3 Effects of salt

With initial concentration adjustments proving ineffective, we explored the impact of varying salt concentrations. A moderate salt concentration in buffer solution is known to have a 'salting in' effect, shielding the charges and improving solubility [85]. hIAPP-S29P was aggregated in Tris-HCl at pH 7.4 buffer with 0 mM NaCl, 50 mM NaCl, 300 mM NaCl, 500 mM NaCl, and 800 mM NaCl.

Nevertheless, the salt concentration did not appear to help separate the fibrils overall, as shown in Figure 3.2. Instead, all the grids looked similar and the 'salting in' effects were not observed in the hIAPP grids, consistent with another amyloid study [86]. In addition, the aggregation rate of hIAPP increased in response to the increased concentration of salt [87]. Since different salt concentrations failed to reduce fibril clustering, the buffer conditions have been subsequently tested.

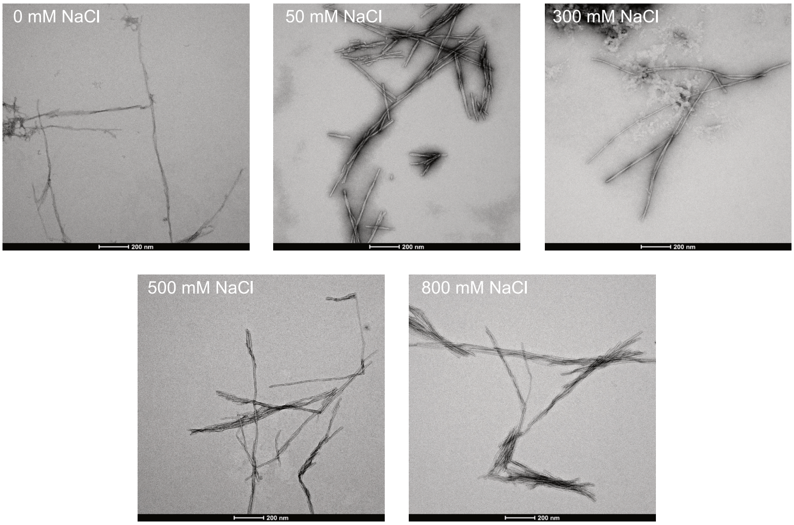

Figure 3.2: hIAPP-S29P aggregated with different concentrations of NaCl in Tris-HCl buffer at pH 7.4 were tested, however, the separation of fibrils did not show a huge difference compared with grids without NaCl. Scale bar: 200 nm.

3.4 Effects of buffers in S29P mutant

The previous conditions were all tested in Tris-HCl buffer as it is one of the most common buffers used to studying the aggregation of hIAPP [88–90]. However, it does not work well for cryo-EM, as the fibrils tend to bundle together and grow spider-web-like, regardless of the initial monomer concentration and salt concentration. After multiple failed attempts, other buffer conditions were tested based on the literature, such as 2-(N-morpholino) ethanesulfonic acid (MES/NaOH) buffer at pH 6 [37] and ammonium acetate buffer at pH 6.8 [38]. Since MES/NaOH buffers well within the range of pH 5.2 to 7.1, an additional condition with MES/NaOH pH 7.1 was also tested. Additional buffers with physiological conditions, including phosphate buffer saline (PBS) and 4-(2-hydroxyethyl)-1-piperazineethanesulfonic acid (HEPES) buffer at pH 7.4 were used as well since studying the aggregation of hIAPP in the physiological environment is favored. The representative negative stained images of hIAPP-S29P aggregated in different buffers are shown in Figure 3.3.

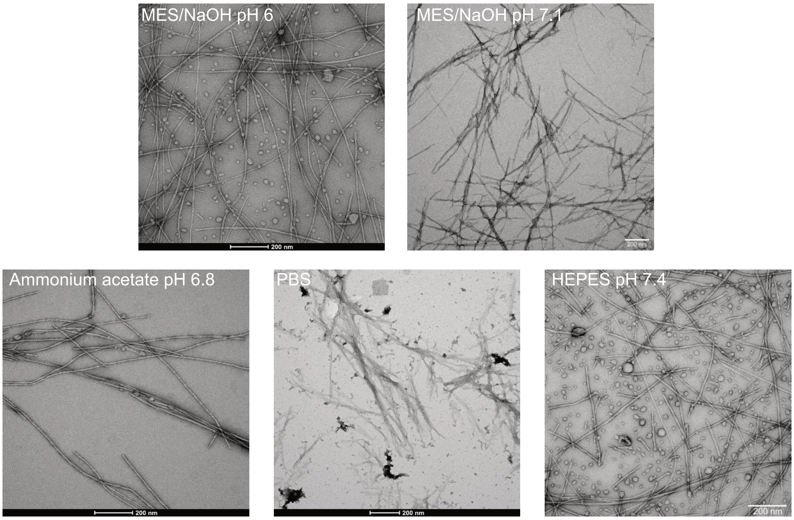

Figure 3.3: hIAPP-S29P aggregated with different choices of buffers were tested. Fibrils aggregated in MES/NaOH at pH 6 and HEPES at pH 7.4 showed good distribution overall and were not bundled together. Scale bar: 200 nm.

Given that fibrils aggregated in MES/NaOH at pH 6 and HEPES at pH 7.4 exhibited superior distribution and more pronounced twisted features compared to other buffers on negatively stained grids, it was hypothesized that morpholine- and piperazine-based organic buffers might offer a better alternative to Tris. Consequently, these buffers were selected for ongoing cryo-EM screening. The representative grid holes and screening micrographs are shown in Figure 3.4. Fibrils aggregated in Tris-HCl buffer were also prepared to allow a comparison between all three buffers in cryo-EM. The Tris-HCl, as expected, showed large amounts of clumps like their negative stained grids. Moreover, they also had thicker ice around the grid hole and extremely thin ice or almost empty in the middle of the grid hole. On the other hand, MES/NaOH and HEPES grids had a similar distribution of fibrils and were rather well separated; however, the ice thickness on the

MES/NaOH grid was thicker and uneven in comparison to the HEPES grid. Thus, the data collection of hIAPP-S29P was continued with a grid prepared with fibrils aggregated in the HEPES buffer.

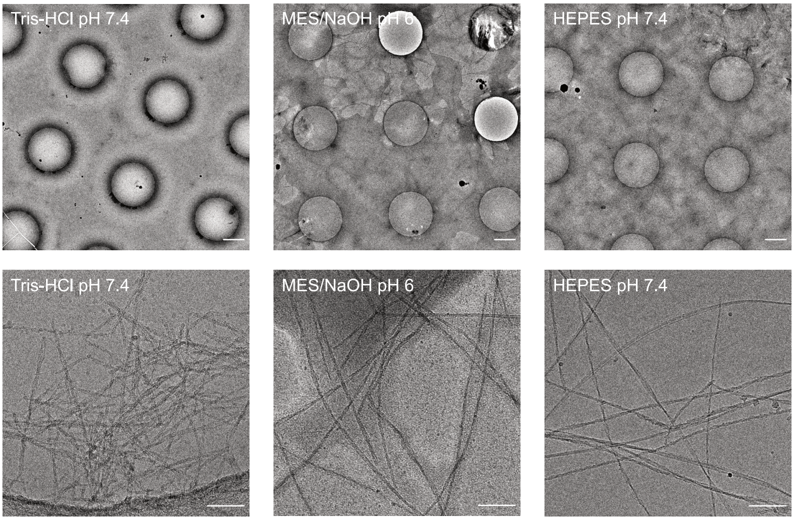

Figure 3.4: Effects of the buffer on hIAPP-S29P cryo-EM grids. Grid holes and acquisition representative of various buffers. HEPES at pH 7.4 showed the best ice layer of all from the grid holes. hIAPP-S29P aggregated in HEPES at pH 7.4 was chosen to acquire the data as it is shown to have the best grid overall in terms of fibril distribution and ice thickness level. Scale bar: 100 nm.

3.5 Effects of buffers in the WT grids

The quality of cryo-EM grids in terms of the fibril distribution and overall ice thickness is highly dependent on the choice of buffer. Additionally, the initial concentration required is also lower, as 50 µM peptide was used in those cryo-screening grids. These results have sparked further investigation into the factors contributing to this significant change. Besides grid quality, it was easier to investigate polymorphs formed under different buffer conditions in WT hIAPP since there are previously solved structures available for direct comparison. Notably, a dominant polymorph of hIAPP-WT has been solved from every buffer condition [37–39], except for the fibrils aggregated in MQ-water [40].

Three buffers chosen to test with WT were: Tris-HCl at pH 7.4, MOPS at pH 6.5 and pH 7.4, and HEPES at pH 7.4. Instead of using MES buffer at pH 6, 3-morpholinopropane-1-sulfonic acid (MOPS) was used as the MOPS buffer ranging from pH 6.5 to 7.9, which spans to the physiological pH. Similar interactions are expected for MES and MOPS buffers since they only differ by a single methylene group separating the morpholine ring from the sulfonate head group. Interestingly, both WT and hIAPP-S29P fibrils aggregated at MES and MOPS at pH 7 and above were bundled together and the ice thickness was poor as well. Figure 3.5 showed that WT fibrils in Tris-HCl at pH 7.4 were bundled as expected, whereas fibrils aggregated in MOPS at pH 6.5 showed good separation of fibrils and decent ice thickness, and fibrils from HEPES at pH 7.4 were well separated and with appropriate ice layers.

An additional challenge emerged during the WT grid optimization. Besides the clumping on grids, the fibrils also favored the carbon support instead of the grid holes with ice. The grid type used was changed from Quantifoil R 2/2 to Quantifoil R 3.5/1 while investigating the effect of buffers on WT grid preparation. The grid hole of 3.5/1 is almost double the size of 2/2, which also reduces the carbon surface area. However, the fibrils still adhered to the carbon support whenever possible, but it provided a higher chance of having the fibril on the grid holes with the bigger grid holes, thus the grid optimization continued with 3.5/1 grids.

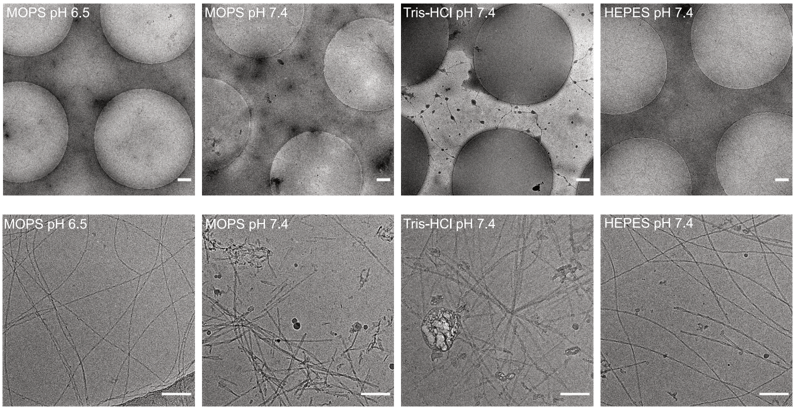

Figure 3.5: Grid squares and grid holes representative for hIAPP-WT in various conditions. The grid with HEPES at pH 7.4 showed the most promising results. Scale bar: 100 nm.

The composition of buffers affects the grids to a great extent; even within the same component but with a different pH, the grids showed completely different behavior. It has been hypothesized that HEPES may behave like a surfactant at 10 and 25 mM concentration [91], which is the concentration that has been used for aggregating the fibrils. This could be why the fibrils were separated well, as the presence of HEPES might reduce the AWI problems. To further investigate the potential surfactant effects, buffer exchange has been carried out by treating HEPES as a surfactant. Fibrils aggregated in Tris-HCl at pH 7.4 are always bundled together and with bad ice thickness, thus it is a good sample for checking the improvement on the effects of the additive on improving the grids. After the fibrils have been aggregated in the Tris-HCl buffer, the HEPES buffer is added into the same solution before freezing the grids. The final concentration of HEPES added was 10, 25, and 50 mM.

Additionally, surface tension measurements were performed to investigate the buffers used. The measurements indicated that Tris-HCl and HEPES have very similar measurements to water; yet water is not a good buffer for grid preparation. Thus, confirming the potential that the effects of HEPES as a surfactant are probably not the only reason why the grids prepared with HEPES are superior.

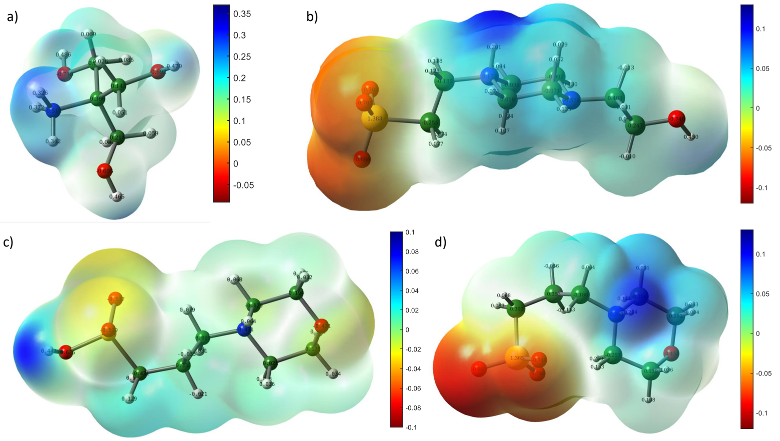

Figure 3.6: Electrostatic potential maps of a) protonated Tris-HCl, b) zwitterionic HEPES, c) neutral MOPS, and d) zwitterionic MOPS calculated with density functional theory using B3LYP function [92] and 6-311+G(d,p) basis set [93–96].

The electrostatic potential maps of Tris-HCl, MOPS and HEPES were calculated with density functional theory using the B3LYP functional [**?**] and the 6-311+G(d,p) basis set

The *ab initio* calculations of the buffer molecules were carried out to compare the electrostatic maps (Figure 3.6). Being zwitterionic buffers, HEPES and MOPS at pH 7.4 have positive and negative charges with similar regions, while Tris-HCl mostly showed positive charges. Both MOPS and HEPES can form hydrogen bonds through their respective sulfonate and amine groups, yet HEPES has an additional hydrogen bonding interaction through its terminal hydroxyl group. Given that HEPES grids are always better, the terminal hydroxyl group in HEPES seems to be crucial in providing fewer clumps and better ice thickness.

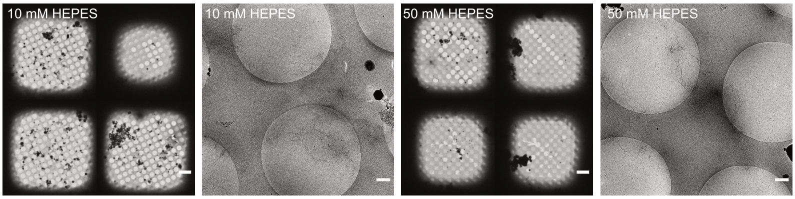

Figure 3.7: Overall 50 mM HEPES provided a better ice layer when treated as a surfactant. Combined grid squares scale: 10 µm. Grid squares scale: 500 nm.

In addition to buffers, the sequence of hIAPP could be affecting the ice as well, as the N-terminal consists of a TxT motif with a non-conserved amino acid between two threonines. This motif is commonly found in antifreeze and ice-nucleating proteins [97, 98], and when they aggregate, ice nucleation is promoted instead of being prevented. Thus, the presence of bundled fibrils provides a nucleation site for ice formation. This could be the reason why the grid prepared in buffers other than HEPES usually consists of poor ice, as the chemical property of HEPES might have a specific interaction with the ice nucleation sites. As shown in Figure 3.7, the ice has improved in response to the concentration, since 50 mM HEPES showed the most improvement; however, the fibril clumping issues persist.

3.6 Effects of additives

This has led to an additional buffer exchange test with the use of detergents to create a monolayer on the surface. When SDS at 2 mM, which is below critical micelle concentration, was added to the solution, it produced the most stable ice layer among all conditions that have been tested so far. This could potentially be due to the detergents forming a monolayer on the surface of the ice and reducing the surface tension fluctuations. However, the fibrils are still clumped together with a small improvement of separation and most fibrils still tend to stay on the carbon support.

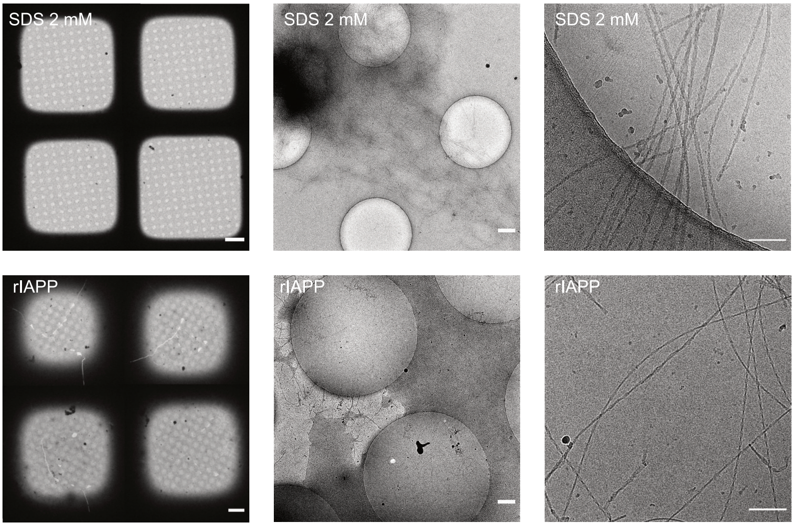

Figure 3.8: The addition of SDS before freezing the grids has improved the ice thickness, and with the addition of rIAPP the distribution of fibrils has been separated. Grid square scale: 10 µm, grid holes scale: 500 nm, and acquisition scale bar: 100 nm.

Other than detergents, there have been studies where denatured protein could be used as an additive to improve the AWI effect [99]. In addition to being a disordered peptide and not aggregating in physiological pH, rIAPP consists of polar and non-polar domains, which could behave like a surfactant. Thus, a low concentration of rIAPP (25 or 50 µM) was added to the fibrils aggregated in Tris-HCl. Figure 3.8 shows improved ice layers and fewer clumped fibrils compared to Tris-HCl grids without rIAPP. Indeed, the addition of rIAPP provided good ice thickness and even well-separated fibrils. As discussed earlier, the surfactant property alone from SDS is insufficient to separate the fibril. Thus some specific interactions between rIAPP and hIAPP helped separate the fibrils, which could be described based on a previous molecular dynamics study [100]. The N-terminal rIAPP, between residue 10 to 18, has the strongest stabilizing energy when interacting with hIAPP. With the N-terminal of rIAPP interacting with hIAPP fibrils, the other parts of rIAPP potentially prevented the presence of other fibrils at close distances. rIAPP has been known to inhibit or cross-seeding of hIAPP [101, 102], however, rIAPP is added before the freezing with already formed fibril, so the potential of cross-seeding should be low. Even though the ice thickness improvement is not as great as the addition of SDS, rIAPP provided the best overall improvement on the grids.

3.7 The dominant structure of WT found in other published articles

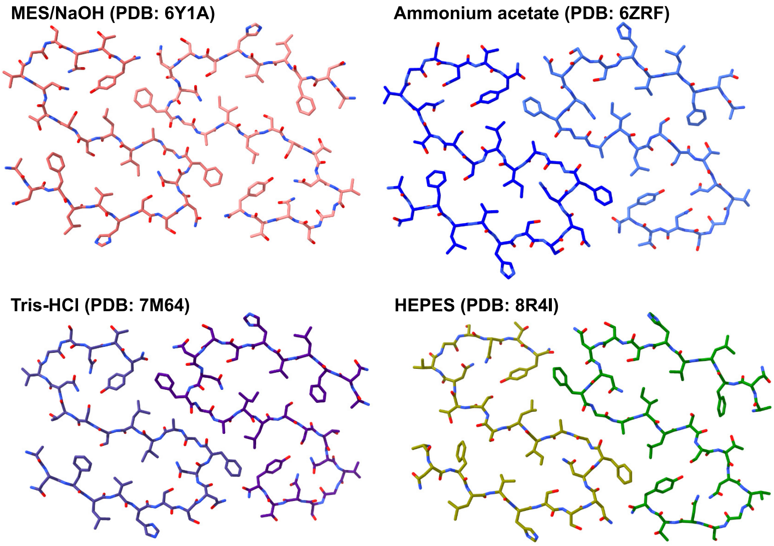

Figure 3.9: Comparison of the dominant polymorph (SS) of WT solved across the literature. The structures are rather identical, with some rotamers, even though they are solved from different aggregation conditions.

Fibril formation has always been easily influenced by experimental factors, like pH, buffers, temperature, agitation, and even the presence of other additives or proteins [103, 104]. An example is the aggregation of tau amyloid that leads to neurodegenerative diseases, with one of them being Alzheimer's disease. In fact, Tau amyloid has very different fibril structures when aggregated in different buffer conditions [105, 106].

It is common for amyloid fibrils to have polymorphism. However, since the fibril formation tends to be affected by external factors, the same structure might not be found in another aggregation condition. Yet for hIAPP WT, a dominant polymorph has been reported across several literature which were aggregated in different conditions and pH as shown in Figure 3.9. The same dominant polymorph was also discovered in WT aggregated at HEPES at pH 7.4 as shown in Figure 3.10. The described twist and rise parameters were used to reconstruct the particles, and the final map was refined up to 4.011 Å. To further confirm the structure, a published PDB

(7M64) was fitted into the map and refined. Most of the amino acid residues fitted well, exhibiting rotamers of Phe15 and His18 residues.

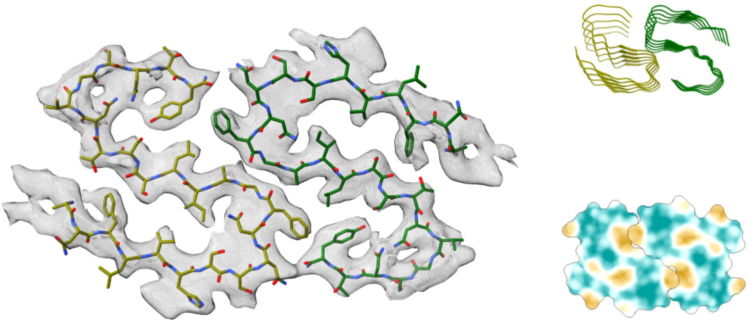

Figure 3.10: The dominant polymorph of WT solved in HEPES buffer at pH 7.4 with a resolution of 4.011 Å. The beta sheets are shown on the top right and the hydrophobicity of the structure is shown on the bottom right.

3.8 Summary

This chapter summarizes the parameters that could improve the grid optimization for cryo-EM, especially for fibrils. The choices of the buffer have the most impact on the ice thickness on the grids, as HEPES provided the best grid for both S29P and WT overall.

However, HEPES alone cannot improve the ice thickness and clumping of fibrils when treated as additives. Previously, the addition of surfactants has been shown to improve the grids and reduce AWI problems. When a low concentration of SDS was added prior to freezing, the ice layers improved tremendously, but there was only minor improvement in separating the fibrils. Instead, the addition of rIAPP as a surfactant showed the best overall improvement. The findings could provide insight into other proteins' grid optimization since small proteins like rIAPP, in general, do not affect the image analysis as they are small enough to be ignored by the microscope. The effects of HEPES buffer, SDS, and rIAPP on grid optimization and the dominant hIAPP-WT polymorph solved in HEPES buffer at pH 7.4 are included in **paper I**.

Chapter 4

Effect of Site-Specific Proline Mutations on hIAPP Fibril Formation

Pramlintide was developed to assist patients by regulating their blood sugar levels and reducing appetite, which, in turn, can lead to a reduction in body weight. However, due to its chemical properties, Pramlintide was formulated at a different pH than insulin, and its short half-life makes it less appealing for use. Nevertheless, the reason behind Pramlintide being non-amyloidogenic with three proline mutations from rIAPP is intriguing. In the pursuit of understanding how site-specific mutations inhibit amyloid formation in Pramlintide, we have conducted extensive experiments with IAPP containing single proline mutations. This approach is aimed at deciphering the critical role of specific residues located in the amyloidogenic core of IAPP. Through these targeted investigations, the aim was to unravel the molecular mechanisms behind the non-amyloidogenic properties of Pramlintide. Additionally, these studies hold the promise of identifying key residues, potentially leading to the development of an improved drug formulation with enhanced solubility, suitable for co-formulation with insulin. The methodologies employed encompass kinetic studies of proline mutants and structural analyses using cryo-electron microscopy (cryo-EM). Given the need for detailed atomic information, cryo-EM is the preferred technique for this research. It surpasses negative stain electron microscopy in resolution, allowing for a more refined exploration of different polymorphic structures.

4.1 How proline mutations affect the aggregation process?

In hIAPP, the amyloidogenic core region spans from N20 to S29, with ^{23}FGAIL^{27} region being the most critical [107]. rIAPP has six differences in the amino acid sequence compared to hIAPP, three of which fall within the FGAIL region and it does not aggregate under physiological conditions. Non-aggregating and soluble forms of IAPP are desirable therapeutic agents. Pramlintide, an IAPP analog, has been designed based on some differences between the rat and human sequences, with three prolines mutating at positions A25, S28, and S29. This drug has better solubility at lower pH in comparison with hIAPP and has been used as a complementary drug together with insulin to treat type 2 diabetes [108].

Figure 4.1: The sequence alignments of hIAPP WT, rIAPP, Pramlintide, mutants A25P, S28P, and S29P.

In this chapter, the significance of the amyloidogenic core region in fibril formation was explored by introducing proline mutations based on Pramlintide. Proline is recognized as a β-sheet breaker, disrupting the hydrogen bonding network. To study the effect of proline in specific positions, single proline mutations were individually introduced on the WT sequence, i.e. hIAPP-A25P, -S28P, and -S29P. This allows the investigation of how each proline mutations affect the formation of the intermediate, the overall aggregation process, and the final structure of the fibrils. Introducing mutations disrupts the normal pathways that lead to fibrils, creating new interactions between the residues that may alter the folding kinetics and the final structure. The sequences of WT, rIAPP, Pramlintide, and the mutants are shown in Figure 4.1.

The mutants (A25P, S28P, and S29) of hIAPP were synthesized using SPPS, and their masses were confirmed with LC-MS. The formation of the

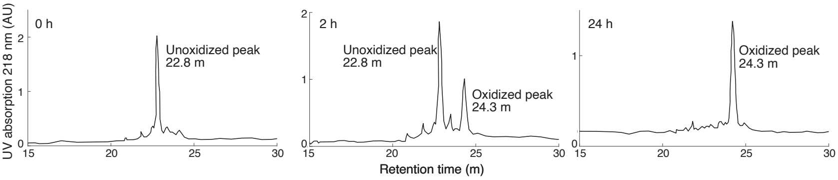

Figure 4.2: The HPLC chromatogram of S28P at 0 h, 2 h and 24 h. The DMSO oxidation of the disulfide bridge of mutant S28P-hIAPP over 24 hours. The peak from 24.3 m was collected and lyophilized.

disulfide bridge was achieved through DMSO oxidation and was confirmed by LC-MS. Figure 4.2 illustrates an example of the disulfide bridge formation for S28P using DMSO over 24 hours. The reverse-phase purification method allowed easy differentiation between unoxidized and oxidized peptides. The first peak (22.8 m) from both 0 and 2 h represented unoxidized S28P, while the second peak (24.3 m) from both 2 h and 24 h represented oxidized S28P. The second peak was collected and lyophilized overnight to remove the solvent. All the synthesized peptides exhibited correct masses based on LC-MS, as shown in Figure 4.3.

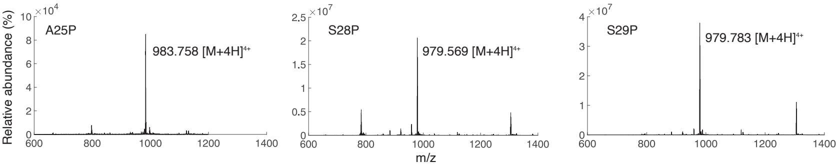

Figure 4.3: Synthesized peptide masses were confirmed with LC-MS. Molecular weight: a) A25P 3932 g/mol, b) S28P 3912 g/mol and c) S29P 3912 g/mol.

4.2 Single proline mutation fails to inhibit aggregation

The aggregation kinetics were investigated with ThT to explore the potential of single proline inhibiting the formation of fibrils. As shown in Figure 4.4, all three mutants exhibited fibril formations, with the intensity increasing and reaching a plateau at the end of the measurements. The curves followed a sigmoidal shape, indicating that the aggregation initiated from a monomeric state in all measured samples.

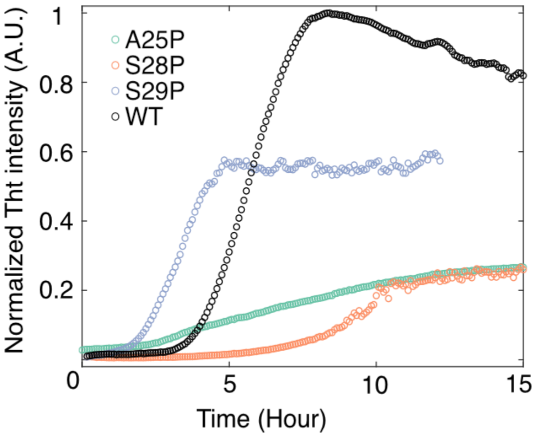

Figure 4.4: The aggregation kinetics of WT and mutants that have been followed *in vitro* with ThT. S29P has the fastest aggregation followed by WT, A25P, and S28P.

Despite displaying a weaker plateau signal than the WT, S29P aggregated the fastest and appeared to have the least affected by the proline mutation. Interestingly, with the same mutation from serine-to-proline as S29P but at one position apart, S28P was the most affected, showing extremely slow aggregation kinetics and the weakest fluorescence signal. On the other hand, A25P has a distinctive curve, displaying slower aggregation with an extended elongation phase, contrasting with the typical short elongation phase observed in S29P.

Explaining how certain mutations have slower kinetics than others based solely on WT structures is challenging. A study conducted with double proline mutations of A25P and S29P indicated that two proline mutations do not necessarily completely inhibit aggregation [109]. However, a double proline mutation with S28P did completely inhibit the aggregation, suggesting that the position of S28P is highly affected by the mutation.

Therefore, understanding the important interactions that hold the structure, especially when proline is introduced, is crucial. The polymorphism of the proline mutants is also unknown and it would be beneficial to know the precise structural information to design new alternatives to Pramlintide.

4.3 High-resolution structures of proline mutants solved with cryo-EM

To further confirm the presence of fibrils, negative stain TEM was carried out with the mutants. All three mutants showed typical rod-like features of fibrils under the microscopes, with the potential for polymorphism (Figure 4.5). However, investigating the high resolution of the polymorphism with TEM was difficult. Therefore, cryo-EM was employed to evaluate the effect of proline in the atomic detail of the structures.

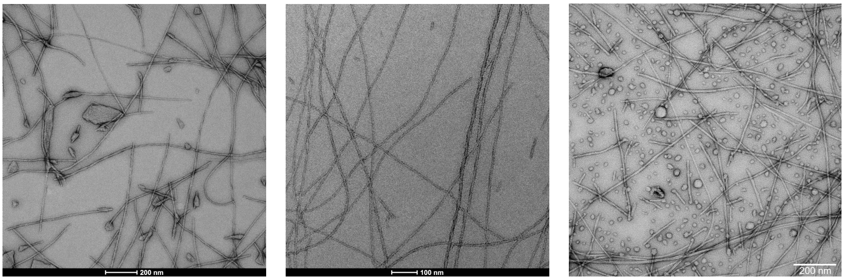

(a) **(b)** **(c)**

Figure 4.5: Negative stained micrographs of a) A25P, b) S28P, c) S29P showing the formation of fibrils, further confirmed with kinetics study results. Scale bar: 200 nm.

Cryo-EM grid optimization of S29P was carried out as described in Chapter 3. Once the optimal condition was determined for S29P, the same condition was applied to the grids for A25P and S28P. Data for S28P and S29P were collected with Titan Krios from Umeå Centre for Electron Microscopy at Umeå University, while the A25P data was collected with Titan Krios at SciLifeLab in Stockholm.

The data were analyzed with RELION (REgularised LIkelihood OptimisatioN), a software for analyzing cryo-EM data [110]. RELION employs the Bayesian statistical method, which improves the accuracy of the reconstructed structures through maximum likelihood estimation and regularization techniques. RELION also features an algorithm specifically developed for reconstructing the fibrils. *Coot* [79] and Phenix [111] were used for building the atomic model and refinement.

During the cryo screening, each mutant was found to have at least two fibril polymorphs. This was confirmed during the 2D classification step, revealing that the fibrils have very distinct appearances and did not share the same polymorph structures among the mutants. In addition, the dominant polymorph from WT was also not found in any of the mutants. The class

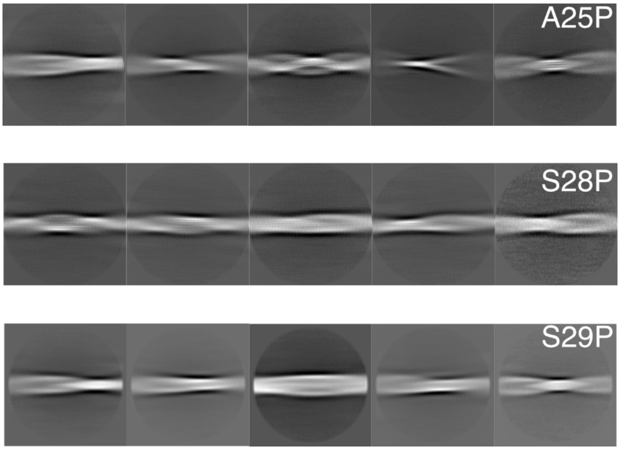

Figure 4.6: The top five twisted 2D class averages for each mutant, which have very distinctive polymorphs. Especially between S28P and S29P with only one position difference yet producing very different average classes.

averages of the top five polymorphs are shown in Figure 4.6. Solving every single polymorph was challenging due to the time-consuming nature of structure determination, the heterogeneity of the structures, and sometimes an insufficient number of particles for reconstruction after multiple classifications. The structures solved from the data will be described below, with each polymorph labeled as the mutant followed by Polymorph 1 (P1), P2, and so on.

4.4 Structures of hIAPP-A25P

Two high-resolution structures were solved from A25P data. hIAPP-A25P P1 mutant is a trimer with a C3 rotational symmetry (Figure 4.7). While a trimer is not an uncommon structure in amyloid fibril, this represents the first trimer structure solved in hIAPP amyloid with C3 symmetry.

The structure is stabilized by Phe23 from each protofilament forming a hydrophobic core, further enhanced by the hydrophobic interaction between Ile26 and Tyr37. The β-sheets are formed by Thr6-Leu12, Phe15-Asn22, Ile26-Asn31, and Gly33-Thr36. Beyond the hydrophobic interaction, the β-sheets are stabilized by the ladder-like interactions involving Gln10, His18, Asn21, and Asn22. Numerous hydrogen bonds contribute to the overall stability, including those between Ser20 and Tyr37 (two layers below), Thr30 with Asn35, and Asn35 with Tyr37.

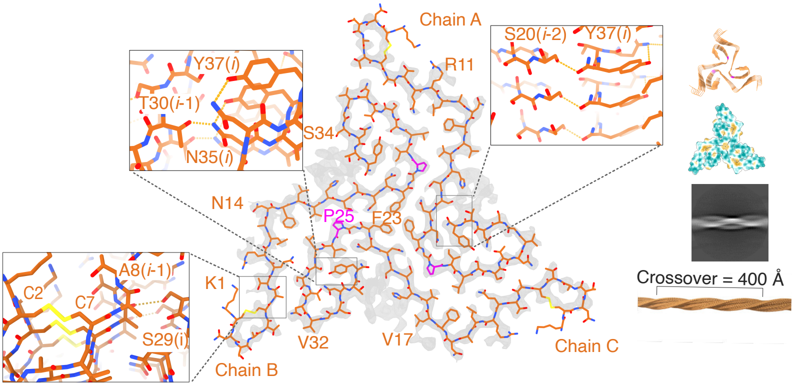

Figure 4.7: A25P P1: a trimer with C3 symmetry, with three Phe23 interacting with each other forming the core. A disulfide bridge is seen between Cys2 and Cys7. Tyr37 interacts with its own Asn35 and Thr30 from the layer below.

Despite the flexible N-terminal in hIAPP, which is usually described as the flanking regions, the first ten amino acids are clearly observed in A25P-P1, with the entire sequence modeled. Notably, Arg11 and His18 exhibit rotamers in this structure. The mutation of Ala25 to Pro25 facilitated the structure by bringing three phenylalanines together, forming a strong hydrophobic interaction.

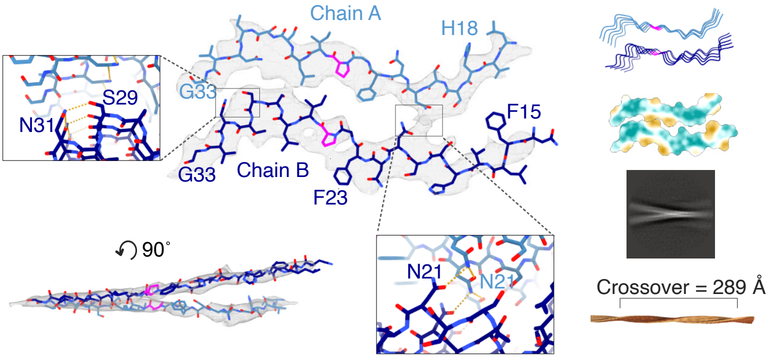

Figure 4.8: A25P P2: a polymorph with an almost parallel arrangement of the protofilament from the top view. Asn21 from chain A forms hydrogen bonding with Asn21 from chain B. Within chain B, Ser29 interacts with Asn31.

For hIAPP-P2, it has an intriguing structure where two protofilaments align to each other in parallel from the top view, but there is almost a β-sheet difference between the two protofilaments on the side view (Figure 4.8). The unique 2D class average resembles a 'Y' character, probably coming from a flexible N-terminal flanking region and potentially a more flexible C-terminal compared to other structures. In chain A, the layers are stabilized by a ladder-like feature formed by Asn21 and Asn31. Asn21 forms its own ladders and also forms hydrogen bonds with Asn21 from chain B. In chain B, only Asn31 forms the ladders while forming a hydrogen bond with Ser29, further stabilizing the structure. Additionally, there is also hydrophobic interaction between the protofilaments, involving Phe23 and Leu27 from chain A with Ile26 from chain B.

4.5 Structures of hIAPP-S28P

For hIAPP-S28P, the 2D classifications revealed polymorphs that differed in overall appearances and cross-over distances. However, several 2D class averages seemed to converge towards a similar 3D initial model, suggesting a limited number of conformational arrangements and a common structural motif, despite different cross-over distances and the overall appearance of the 2D class averages. Unfortunately, only two structures were solved for the S28P mutant, although a sufficient number of particles was available for refinement of other structures. This suggests a high degree of heterogeneity or flexibility along the fibril axis, or potentially multiple different 2D class averages converging to the same 3D structure. The final two structures solved to high resolution, namely P1-α and P1-β, displayed very high similarities despite originating from different 2D class averages. The main difference is that in P1-β, the position of the proline is oriented towards another direction due to the shift of the amino acids after residue 20.

This observation may explain the slower aggregation kinetics of the S28P mutant, as the aggregation process must be directed toward a specific, dominant structural motif. In contrast, the large number of polymorphs formed by other mutants may give the impression of faster aggregation kinetics, especially when a specific polymorph forms more quickly than others. It also indicates that, for certain peptides, 2D class averages alone may not suffice for accurate particle classification, since polymorphs with different cross-over distances can still form similar 3D structures.

In Figure 4.9 top part, hIAPP-S28P P1-α has a unique structure where the C-terminus of chain A is somewhat buried by chain B. Tyr37 from chain A is surrounded by chain B, stabilized by the hydrogen bonding between Tyr37 and Thr30. Additional hydrogen bonding between Pro28 backbone oxygen with Thr30 and Tyr37 further anchors the position of Tyr37. In chain B, Pro28 is more spread away and Asn35 forms the hydrogen bonding with

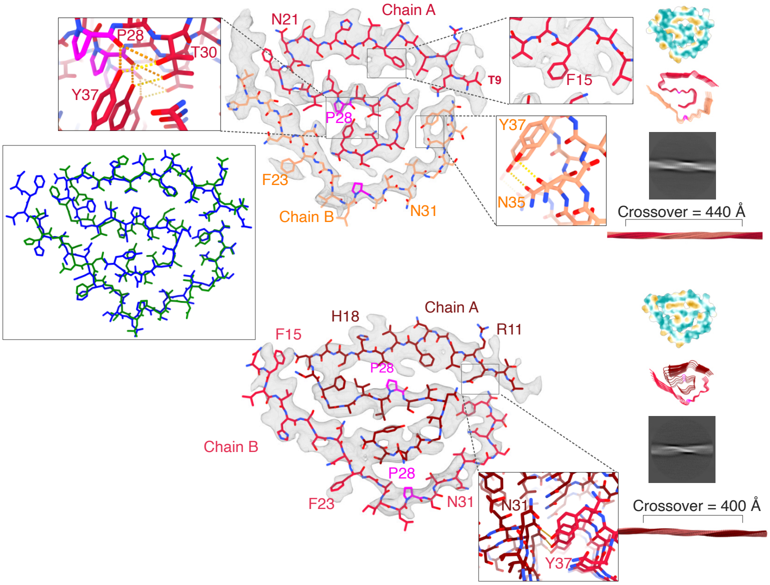

Figure 4.9: S28P: two similar structures are solved from this mutant. The top structure is P1-α with the bottom structure being P1-β. On the middle left, the alignment of S28P-P1-α (blue) and S28P-P1-β (red) shows a rather similar backbone position, with differences around chain B of S28P-P1-β (red). S28P-P1-α's Tyr37 interacts with the oxygen backbone of Pro28, whereas S28P-P1-β's Tyr37 interacts with Ser34.

Try37, while Val32 from chain A provides hydrophobic interaction with chain B Tyr37.

The residues are fitted from Thr9 to Tyr37 in chain A and Val17 to Tyr37 in chain B. Chain A Asn31 forms ladder-like stabilization between the layers. The β-sheets for chain A are from Gln10 to Ala13, Phe15 to Ser20, while for chain B, they range from His18 to Phe23 and Gly33 to Thr36. Two rotamers (Phe15 and His18) from chain A are observed in the density.

In Figure 4.9 bottom part, S28P P1-β has a different interaction in chain A C-terminus. Tyr37 forms a hydrogen bond with Ser34 within the protofilament. Unlike the P1-α structure, the backbone oxygen of Pro28 does not provide any interactions it faces another direction. Gln10 from chain A also interacts with Tyr37 from chain B. The hydrophobic core of chain A is stabilized by Leu27 and Tyr37.

In chain A, the residues are fitted from Ala8 to Tyr37, whereas in chain B, they range from Asn14 to Tyr37. Asn 14 and Asn22 from chain B also form the ladder-like interaction. On top of that, rotamer densities are visible for both Phe15 and His18 from chain B. The β-sheets for chain A span from Thr9 to Leu12, Phe15 to Ser20, and Phe15 to Asn22 in chain B.

4.6 Structures of hIAPP-S29P

Three polymorphs were solved from S29P. S29P-P1 has a C2 symmetry where the residues are fitted from residue Ala8 to Tyr37 (Figure 4.10). The core of the structure has a steric zipper interaction spanning from Phe15 to Phe23, supported by an extensive network of hydrogen bonding. His18 forms hydrogen bonds with amino acids (Ser20, Asn31) from the layer below it, while Ser19 also forms a hydrogen bond with Asn21 from another protofilament. Within the same chain, Asn14 forms a hydrogen bond with the backbone oxygen of Thr36, and the backbone oxygen of Phe15 also forms a hydrogen bond with Asn35 from the two layers below.

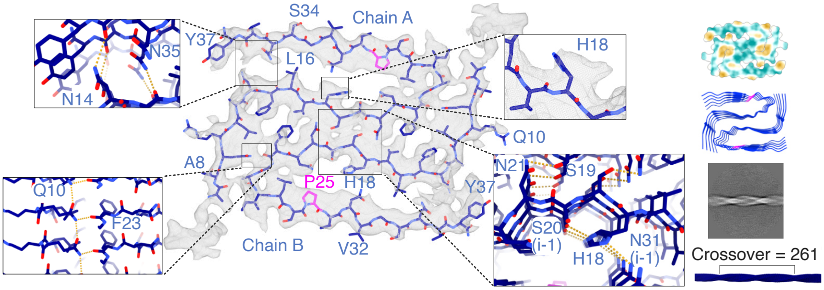

Figure 4.10: S29P P1: a C2 symmetry structure with an extensive network of hydrogen bonding in the core of the structure. Asn21 from chain A interacts with Ser19 from chain B. His18 from chain A interacts with Ser20 and Asn31 from one layer below.

The N-terminus is stabilized by Gln10 forming a hydrogen bond with the backbone oxygen of Phe23 from another chain, and hydrophobic interactions from chain A Phe15 and chain B Leu12, Phe15, and Val17 support the turn of the β-sheets. Additionally, the structure is further stabilized by the ladder-like forms of Gln10 and Asn22. The β sheets span from Gln10 to Leu12, Asn14 to Ser19, and Thr30 to Ser34. His18 displays a rotamer in this structure.

As shown in Figure 4.11, S29P-P2 is a trimer that almost has a C3 symmetry, with chains A and B being similar, while chain C has a different amino acid that contributed to the core, namely Leu27. Hydrophobic interactions from two Phe23 and single Leu27 hold the core of the structure. An

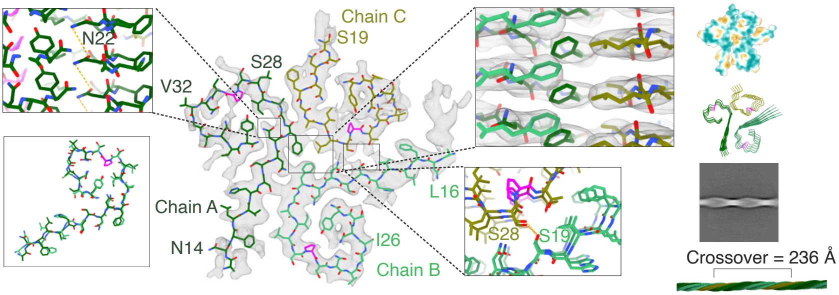

Figure 4.11: S29P P2: a trimer with a C1 symmetry. Chain C has a shorter chain which Leu27 contributed to the hydrophobic core, in contrast to Phe23 from chains A and B. The alignment of chains A and B shows almost identical protofilament with some side chain rotamers.

additional hydrogen bond between chain A Ser28 and chain B Ser19 stabilizes the structure. The typical ladder-like is also observed in Asn21 from chains A and B, and Asn22 from chain C.

Chain A and B are almost identical in the backbone when aligned, with some residues having different rotamers. Interestingly, chains A and C are on the same level of layers, while chain B is in between the two layers of fibrils. Residues are fitted differently in each chain, with chains A and B ranging from Asn14 to Tyr37 and chain C from Asn21 to Tyr37. The β-sheets are observed from Asn14 to Phe 23 for chain A, Asn14 to Phe23 (with a short one between Ile26 to Leu27) for chain B, and also a short one between Ile26 to Leu27 for chain C.

S29P-P3 resembles the TW4 structure (PDB: 7M65), with a flipped domain on the right side of the fibril compared to the published structure (Figure 4.12). Residues are fitted from Lys1 to Tyr37 on chain A, with a disulfide bridge between Cys2 and Cys7, while the N-terminus is missing on chain B, and the residues are fitted from Leu12 to Tyr37.

The hydrophobic interaction stabilizing the protofilament of chain A comes mainly from Leu12, Phe15, Val17, Ile26, and Leu27, whereas for chain B, it comes from Phe15, Val17, Ile26, Leu27, and Tyr37. Between two protofilaments, there is a hydrophobic interaction between chain A Val32 and chain B Phe23. In addition, the structure is also stabilized by hydrogen bonding between chain A Thr30 and chain B Asn21, and chain A Tyr37 with chain B Ser 28. The ladder-like formation from Asn is also found in this structure with Asn22 and Asn35 in chain B.

The β-sheets for chain A span from Ala8 to Ala13, Phe15 to Ser20, Thr30 to Gly33, and Asn35 to Thr36; there is only β-sheet for chain B, spanning from Asn14 to Ser20.

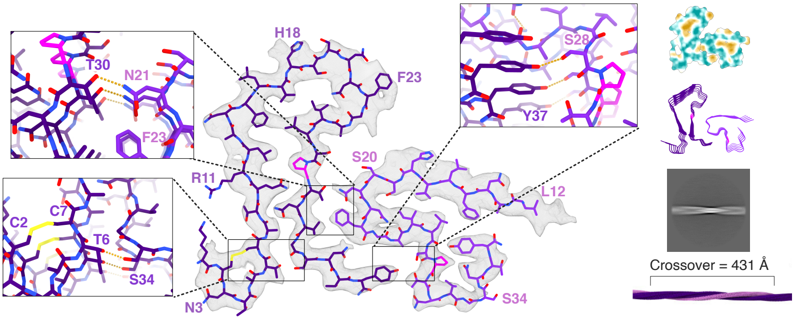

Figure 4.12: S29P-P3: a dimer with C1 symmetry. Chain A is stabilized with hydrogen bonding with Thr6 and Ser34 and the hydrophobic interactions between Phe15 and Leu27. Thr30 from chain A interacts with Asn21 from chain B, in addition to Try37 from chain A interacts with Ser28 of chain B.

4.7 Comparison with published structures

To develop a non-amyloidogenic form of hIAPP, relying solely on the WT structures proves insufficient. Proline mutation studies reveal that certain residues, seemingly unimportant in WT, become crucial in forming a new core when a perturbation is introduced. Additionally, most of the cryo-EM structures of hIAPP published have been either chemically synthesized or expressed *in vitro*. Only one paper, in which the structures were seeded with patient-extracted fibrils [39]. Normally, when a preformed fibril (the seed) is added to a fresh batch of monomeric protein, it induces the formation of fibrils in a structure similar to the seed. This method is particularly useful when patient-extracted samples are challenging to obtain. Seeded structures are expected to resemble the actual fibrils found in the human body [112]. Therefore, the structures solved in this paper are being used as a comparison of the mutant structures.

None of the structures solved in this study resemble any of the WT-seeded structures, even the dominant structure of WT solved in chapter 3. The β-sheets of the WT-seeded and WT in HEPES, alongside with the mutants are compared as shown in Figure 4.13. The β-sheets formed across the structures are not always composed of exact amino acid residues; sometimes they could span from one or two residues before or after in different structures. The β-sheets in WT typically span around residues 7 to 10 or even 15 for the N-terminus, residues 14 to 18, residues 23 to 28 (FGAIL region), and residues 33 to 36 at the C-terminal regions.

As shown in Figure 4.13, the proline mutants form β-sheets rather different from the WT structures. All of the mutant structures formed β-sheets, except A25P-P2, potentially due to the flexibility of the structure. The β-sheets span around the N-terminus after residues 7 to 12 remain similar in mutants, with some structures having shorter β-sheets, such as S28P P1-α and β, and S29P P1.

However, the presence of proline increased the amino acid residues contributing to the β-sheets after the N-terminal regions. For example, in almost all structures in proline mutants, especially A25P-P1 and S29P-P2, they form longer β-sheets around 15 to 23, whereas in the WT structures, they tend to have shorter β-sheets in that region. This change can also be found in the C-terminus, where A25P-P1 and S29P P3 chain A have two β-sheets after the proline mutations and S29P P1 has a longer β-sheet.

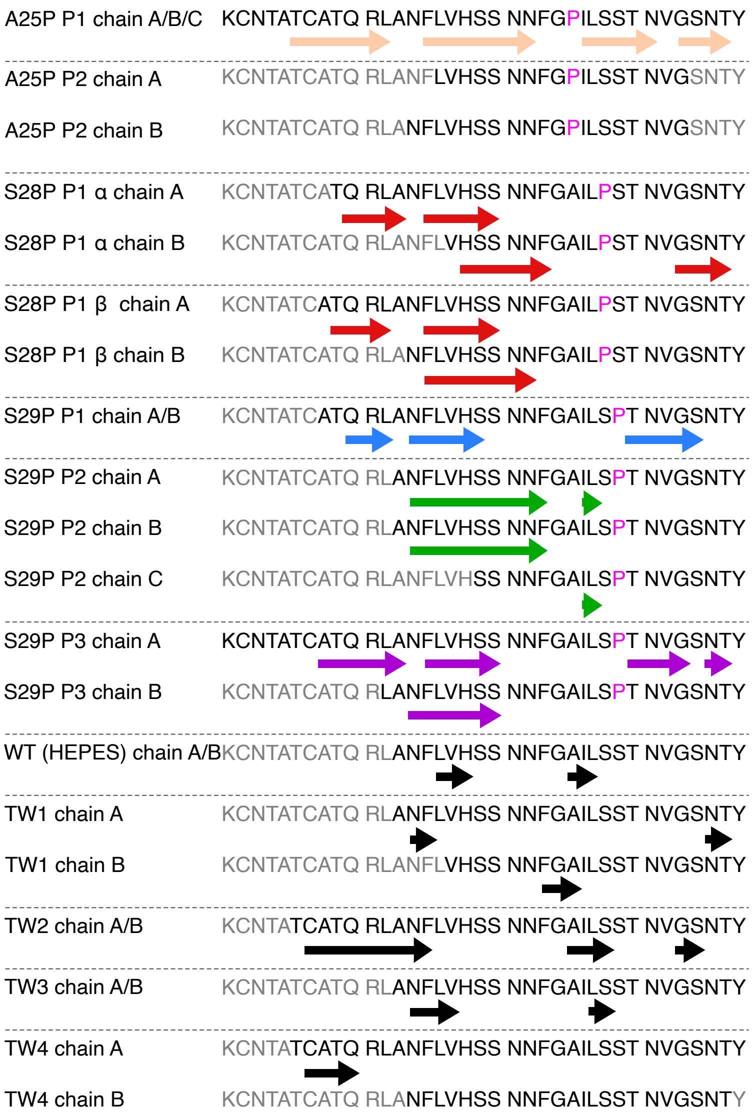

Figure 4.13: The β-sheets comparison between the structures solved in this study and WT structures in HEPES and formed ex vivo. The proline mutation has shifted the positions of the β-sheets away from the FGAIL region but also introduced longer β-sheets in some structures.

The results imply that in the presence of proline, residues that typically do not contribute to the β-sheets could potentially be involved in the formation of β-sheets, aiding in stabilizing the structures. To design a non-amyloidogenic IAPP, it may be necessary to implement at least two mutations to prevent the formation of β-sheets, as shown in studies [113, 114].

4.8 Summary

The majority of published structures so far include hIAPP-WT in different buffer conditions and a mutant with S20G. Proline mutations on hIAPP have formed unique fibril structures that have not been observed in other mutants. Overall the structures solved in this chapter are held together by various interactions such as hydrophobic interaction, hydrogen bonding, and ladder-like. The results from this chapter are summarized in **paper II**.

The proline mutation at position 25 led the Phe23 to interact with other phenylalanines, resulting in a C3 symmetric trimer. A25P-P2 has a distinct structure from A25P-P1, featuring more flanking regions on both N- and C-terminus.

Interestingly, for S28P, the mutant with the slowest aggregation, the two structures solved are rather similar with a slight difference in the direction of the proline in chain A. Despite particles being chosen from different class averages and having different twist values, it appears that one dominant fibril started to form during the aggregation. As the aggregation continued, the second polymorph diverged from the dominant polymorph with small differences.

In contrast, S29P, with the same proline mutation on serine but one position apart, has formed very different structures compared to S28P. This difference is not unexpected, considering that species developing diabetes in nature often have proline on position 29. The ThT kinetics for S29P were almost unaffected by the mutation, or even comparatively faster than the WT. The three structures are also dissimilar to one another. S29P-P2 might have been very similar to A25P-P1 if chain C had Leu27 interacting with the hydrophobic core.

Based on the results from this study, a mutant with F23A and A25P mutation is synthesized to investigate the potential for aggregation. This mutant could serve as a mimetic-drug model for potential drug treatment for type 2 diabetes, offering better stability at physiological pH than Pramlintide. Additional stability assessments of the mutant should be conducted to avoid post-translational modification on the new mutant.

Chapter 5

Effects of buffer composition on the inhibition of rIAPP on hIAPP fibril formation

Designing molecular inhibitors is another promising strategy in the development of therapeutics against the aggregation of hIAPP. The inhibitors for hIAPP can be classified into three classes: small organic molecules, nanoparticles, and peptide mimetics.

The peptide mimetics method has been discussed in the previous chapter. Despite the site-specific proline mutations inspired by rIAPP, hIAPP still aggregates, as demonstrated in the ThT kinetics study. The presence of polymorphism is further confirmed through cryo-EM study. In addition to designing non-amyloidogenic forms of hIAPP, understanding the inhibitory impact on peptide mimetics is equally important. This prompts the investigation into how rIAPP could potentially inhibit hIAPP *in vitro*. As the design of small molecules or peptide-based potential inhibitors becomes increasingly recognized for drug development, this chapter explores the inhibition of hIAPP by non-amyloidogenic forms of IAPP.

5.1 Background

rIAPP has been an interesting target to study alongside hIAPP in elucidating the aggregation mechanism, given its close relation to hIAPP with six amino acid residue differences, yet it does not aggregate in nature. On top of that, rodents such as rats, are among the animals that do not develop diabetes, and share identical sequences with hIAPP for the first 17 and last 8 amino acids, with five of the differences in the amyloidogenic core region (Figure 4.1). Due to the stability of rIAPP in nature, Pramlintide has been designed based on proline mutations from rIAPP as a drug treatment for type 2 diabetes. The introduced mutations on Pramlintide minimally affect binding to amylin receptors while retaining the regulatory properties of hIAPP on satiety.

Notably, rIAPP has been proposed as an inhibitor for hIAPP fibril formation due to the presence of prolines, which are common β-sheets breakers [101, 115]. However, the exact mechanism of the inhibition remains unknown to date. A previous study on the inhibitory effect of rIAPP on hIAPP suggested rIAPP interacts with hIAPP through the N-terminal interactions, potentially diverting the hIAPP off the normal pathway and forming nontoxic oligomers [102]. However, its inhibition effect is lower compared to other small molecule inhibitors [116, 117]. In contrast, insulin typically interacts with monomeric hIAPP for glucose regulation, and it was also found to interact with pre-fibrils of hIAPP [118]. These findings imply the role of insulin in stabilizing the monomeric of hIAPP in the β-cells. The interactions mentioned earlier suggested the potential peptide-induced inhibitory effect on hIAPP, preventing the formation of fibrils *in vivo*.

On the other hand, hIAPP has been discovered to interact with other molecules to form hybrid fibrils, such as Amyloid-β related to Alzheimer's disease [119]. The co-aggregation or cross-seeding of amyloid proteins suggests a poorly understood cross-talk between amyloid diseases. Interestingly, there are studies indicating that while rIAPP inhibits hIAPP, it eventually forms hybrid fibrils containing both hIAPP and rIAPP [120]. However, detailed information on how these hybrid fibrils formed is still unknown, and the current knowledge is solely relying on fluorescence assays. The definite proof for the formation of such hybrid fibrils between closely related peptides could provide valuable insights into the mechanisms of co-aggregation.

In this study, the inhibitory effect of rIAPP and the seeding effect of hIAPP are examined. In the experiments, various concentrations of rIAPP are incubated alongside a constant hIAPP concentration, both originating from monomeric states. To further investigate how the fibril polymorphism of hIAPP is affected by the presence of rIAPP, cryo-EM is employed, offering clear distinctions between different polymorphs during 2D classification. The influence of the solvent affecting fibril formation is also investigated. The findings from this study contribute to a deeper understanding of how hIAPP aggregation can be influenced by a peptide with a similar sequence, as well as by the environment and the presence of small organic molecules.

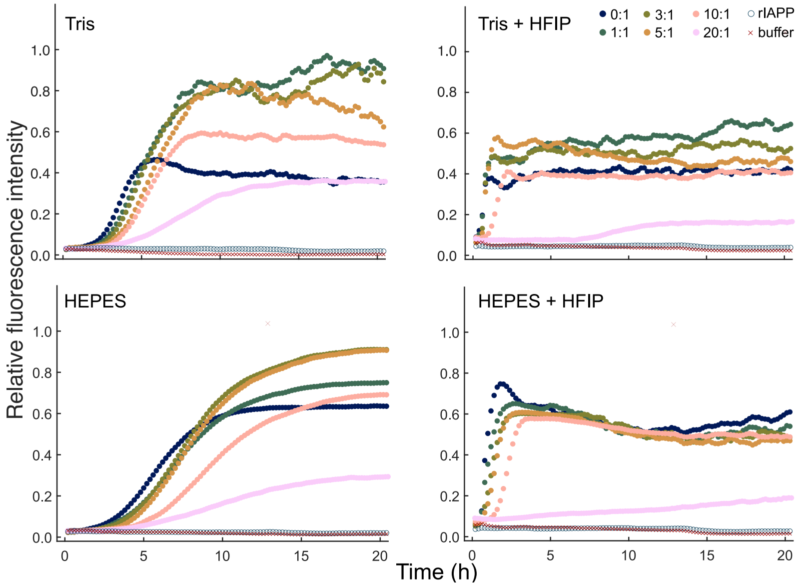

Figure 5.1: The kinetics study of different concentrations of rIAPP on the inhibitory effect of hIAPP fibril formation. The intensities of all fluorescence have been normalized to 1.

5.2 Buffer composition affects the aggregation kinetics

The inhibitory effects of rIAPP on hIAPP have been studied with ThT kinetics. The concentration of hIAPP was maintained at 14 µM, while five concentrations of rIAPP ranged from 14 µM to 280 µM, resulting in ratios of 1:1, 3:1, 5:1, 10:1, and the highest at 20:1. Two buffers, Tris-HCl at pH 7.4 (commonly used in hIAPP studies) and HEPES at pH 7.4 (utilized in previous chapters), were employed to compare the impact of solvents on polymorphism. Additionally, 2% HFIP, a solvent often used to maintain peptide monomerization, was added to explore its influence on aggregation kinetics. Despite its monomerizing role, studies have indicated that HFIP can promote amyloid fibrillation and beta-sheet conformation. This resulted in a total of four buffers at pH 7.4: HEPES, HEPES + 2% HFIP, Tris-HCl, and Tris-HCl with 2% HFIP.

In the HEPES buffer, ranging from 1:1 to 10:1 (rat:human), the kinetics displayed a prolonged lag phase, elongation time, and an overall reduction in ThT intensity, suggesting that an increase in rIAPP concentration moderately inhibits fibril formation. At 20:1 (rat:human), the inhibition was stronger, evident from the lower ThT intensity compared to previous concentrations. In the HEPES with 2% HFIP dataset, aggregation occurred more rapidly, and the intensity decreased, indicating that HFIP accelerated aggregation, leading to the formation of more fibrils.

In the Tris-HCl buffer, the kinetics showed a similar curve but with weaker intensity, suggesting that the inhibitory effect of rIAPP might be more potent in the presence of Tris-HCl. The addition of 2% HFIP in the Tris-HCl buffer also resulted in a faster aggregation process.

5.3 2D class averages to investigate the polymorphism

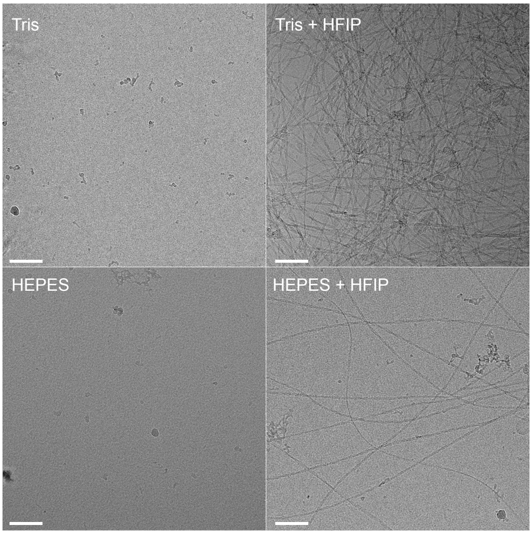

Figure 5.2: Representative micrographs of rIAPP:hIAPP at the ratio of 20:1. Sample aggregated in Tris buffer with the addition of 2% HFIP has the most fibrils.

As the ThT aggregation kinetics yielded distinct results in the presence of HFIP, cryo-EM has been employed to investigate the structure in detail. Approximately 1000 micrographs were collected for the 1:1, 4:1, and 20:1 datasets in four different buffer conditions to investigate fibril population and polymorphism. The representative micrographs of 20:1 are shown in Figure 5.2. Notably, when a high concentration of rIAPP is added to the buffers without HFIP, the observed amount of fibrils is significantly lower compared to other datasets. This suggests that a minimum 20:1 ratio of rIAPP is necessary to inhibit fibril formation. To enable a quantitative comparison of polymorph distribution, fibrils in each dataset were normalized to the total extracted fibrils, and the fibril counts in each dataset were compared in the count column as shown in Figure 5.4.

After the preprocessing of the micrographs, fibrils were manually picked as templates for Topaz autopicking training. All fibrils were picked using the autopicking algorithm, employing a large box size to include longer crossover polymorphs. Figure 5.3 showed the top 25 average classes across all datasets. Notably, a commonly found 2D average class from cryo-EM publication of hIAPP is consistent across all buffers, represented as the first class in Figure 5.3. Interestingly, a polymorph with two parallelly stacked fibrils of the aforementioned polymorph is also found in some datasets. The class averages found range from short crossover to long, elongated, and flat polymorphs. Populations were categorized based on crossover length: below 260 Å, longer than 260 Å, and flat polymorphs.

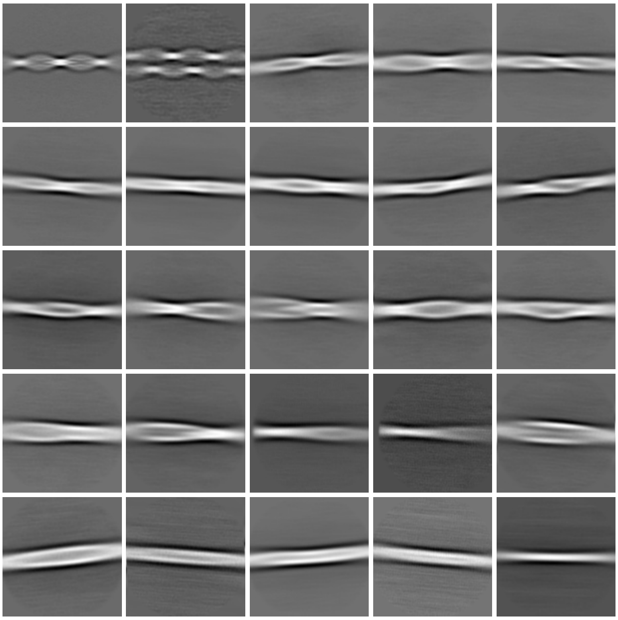

Figure 5.3: Top 25 class averages found from the 2D classifications of image analysis in all datasets.

In the Tris-HCl buffer, a large population of highly twisted fibrils was found at lower concentrations of rIAPP, likely representing the common double S-shaped structure discussed and solved previously in 3. However, the twisted population diminished with increasing rIAPP, replaced by flat and longer crossover polymorphs. This suggests that the highly twisted fibrils may be the dominant polymorph of the WT, as previously discussed.

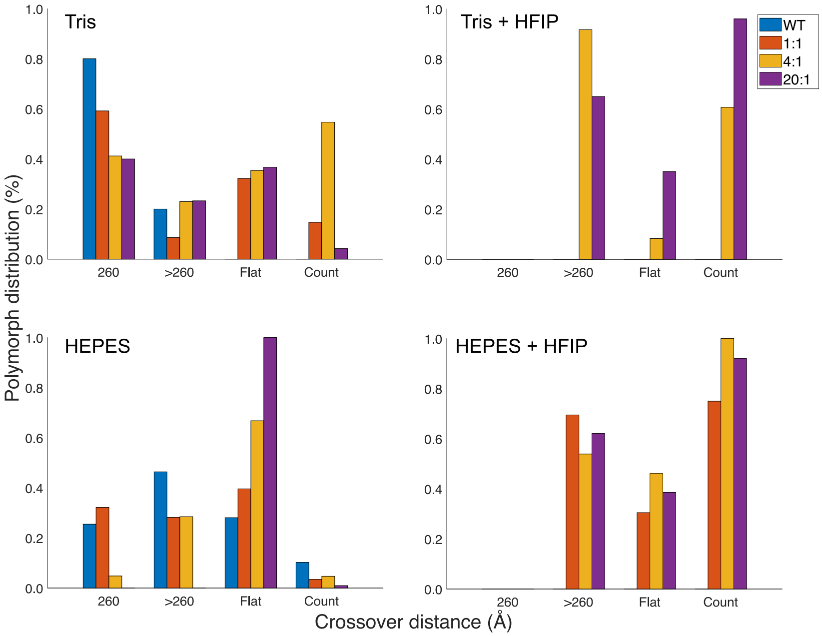

Figure 5.4: Classification of the fibrils according to the crossover distances. For Tris and HEPES, the data with the highest rIAPP concentration gives the lowest fibril amount and also longer crossover distances fibrils. With HFIP added, the data with the highest rIAPP concentration gives the highest amount of fibril instead.

A similar situation is observed in the HEPES buffer, with a slightly smaller population of short crossover polymorphs compared to the Tris-HCl buffer. In both HEPES and Tris-HCl, the dataset with a 10:1 ratio exhibited the highest number of fibrils, suggesting the possible formation of hybrid fibrils between rIAPP and hIAPP, where hIAPP might seed rIAPP rather than being inhibited by it. Conversely, at the 20:1 ratio, fibril amounts were drastically reduced, indicating potential inhibition of hIAPP fibril formation by high concentrations of rIAPP.

Tris-HCl exhibited a higher number of fibrils compared to HEPES only, as fibrils aggregated in Tris-HCl tend to bundle together. The inclusion of HFIP in the buffers led to significant changes, with the 20:1 dataset exhibiting extremely high amounts of fibrils compared to the same dataset without HFIP. Additionally, the short crossover polymorph diminished, and most fibrils displayed longer crossover or flat structures.

5.4 Summary

This chapter summarizes the inhibitory effect of rIAPP on hIAPP fibril formation under different environmental conditions, as assessed through ThT kinetics and cryo-EM. According to the ThT kinetics, it showed that rIAPP only partially inhibits hIAPP when present at concentrations up to ten-fold that of hIAPP. However, the inhibitory effect becomes more pronounced when rIAPP is present at twenty-fold the concentration of hIAPP, as indicated by ThT intensity being only half of the normal level. The micrographs taken at this higher concentration of rIAPP also reveal a significantly lower amount of fibrils compared to other conditions, highlighting a stronger inhibitory effect with increased concentration. This inhibitory effect is observed in both HEPES and Tris buffer. Beyond a certain concentration, the non-amyloidogenic nature of rIAPP proves more effective at preventing the smaller assembly of hIAPP, thereby inhibiting fibril formation.

Nevertheless, below a certain concentration, rIAPP may only be capable of stabilizing alternative structures, resulting in a partial inhibitory effect. The presence of longer and irregular twists observed in the 2D class averages could potentially suggest a hybrid fibril; however, proving this with cryo-EM 2D class averages is challenging. Fibril polymorphism could lead to variations in ThT fluorescence intensity, as different polymorphs provide different binding sites for ThT. Therefore, it is hard to conclude if the high intensity of ThT is due to hybrid fibril in the presence of rIAPP.

On the contrary, buffers containing 2% HFIP yielded significantly different results. Given HFIP's known role in promoting amyloid fibrillation in previous studies, it accelerated fibril aggregation and shortened the lag phase. Notably, even at a high concentration of rIAPP, the inhibitory effect persisted, with ThT intensity lower at twenty-fold rIAPP compared to other datasets. However, cryo-EM confirmed the abundant amount of fibrils formed in twenty-fold of rIAPP, appearing bundled and over-crowded fibrils. Since the detailed mechanism of how ThT binds with β-sheets is unclear, it is potential that crowdedness interferes with the binding, resulting in lower intensity.

In short, the inhibitory effect of rIAPP is concentration-dependent. On the other hand, in the presence of HFIP, the aggregation kinetics are accelerated, leading to different polymorphs. The findings of this study are summarized in **paper III**.

Chapter 6

Concluding remarks and outlook

The study presented in this thesis aims to explore the aggregation of hIAPP *in vitro* from various perspectives, including co-aggregation and mutation analysis. Cryo-EM, a key technique used in this research, is particularly effective for solving high-resolution 3D structures. This is especially true for amyloid fibrils, which pose challenges for other structural techniques due to their heterogeneity and insolubility.

In the first project, efforts have been made to optimize cryo-EM grids containing amyloid fibrils to acquire high-quality data. HEPES buffer produced the best-quality grids, possibly due to its zwitterionic property and the terminal hydroxyl group, which may facilitate specific buffer-peptide interactions. We hypothesize that HEPES buffer may possess unique capability of interacting with the peptide fragments promoting ice nucleation. In the case of bundled fibrils aggregated in Tris-HCl buffer, the addition of a low concentration of rIAPP or SDS surfactant just before freezing significantly improves quality of the grids by stabilizing the air-water interface (AWI). These optimized conditions pave the way for solving multiple high-resolution structures of amyloid fibrils. The use of rIAPP as an additive could also be applied to other amyloid fibrils, or even soluble proteins that struggle to achieve good quality ice.

Developing non-amyloidogenic hIAPP holds promise in diabetes treatment, particularly when weight management is concerned. Site-specific mutations were introduced to understand the molecular interactions, such as hydrogen bonding and hydrophobic interactions in the presence of a β-sheet breaker. Introducing proline into the amyloidogenic core yielded unique structures for each mutant, distinct from known WT structures. For instance, proline at position 25 led to a stable C3 trimer and a more flexible structure, while proline at position 28 resulted in two similar structures. The proline mutation at position 29 formed three distinct structures, one of which resembled a wild-type structure. These solved structures offer fresh insights into amino acid interactions that stabilize fibril architecture in hIAPP.

Recent studies have implemented time-resolved cryo-EM to observe transient conformations of protein structures, which could aid in understanding fibril aggregation. However, this technique is challenging to apply to amyloid fibrils. The aggregation mechanism could be further elucidated using 2D infrared spectroscopy (2DIR), where ^{13}C ^{18}O isotope-labeled amino acids are incorporated into the sequence. This method allows for a detailed investigation of the aggregation mechanism. By combining 2DIR data with cryo-EM structures, a new mutant could be designed to form a soluble, monomeric IAPP homolog for potential drug development against type 2 diabetes.

Several small molecules are known to inhibit hIAPP aggregation, with rIAPP being one of them. Its inhibitory effect on hIAPP fibril formation is concentration-dependent, exhibiting stronger inhibition at higher rIAPP concentrations. The polymorphism of hIAPP fibrils is also influenced by rIAPP concentration, with shorter crossover distances at lower concentrations that transition to longer crossovers as rIAPP concentration increases. The possibility of hIAPP seeding rIAPP to form hybrid fibrils was also investigated. The presence of HFIP in the buffer dramatically altered the dominant species in hIAPP, highlighting the significant impact of environmental factors on hIAPP aggregation. In contrast, rIAPP showed an increase in fibril formation in the presence of HFIP.

Cryo-EM analysis did not provide evidence for hybrid fibril formation in the co-aggregation study of rat and human IAPP, although it is still a possibility. We suggest that the previously observed variations in ThT fluorescence intensity may be attributed to the changes in fibril polymorphism. It is possible that different polymorphs differ by the number of available binding sites for the ThT molecules, which may be mistaken for hybrid fibrils if the intensity increases in the presence of rIAPP in comparison to pure WT peptide. These findings emphasize the importance of utilizing high-resolution techniques like cryo-EM to distinguish between polymorphs, which can exhibit varied intensities and characteristics in other assays.

Overall, this thesis contributes further understanding into the aggregation of hIAPP and lays the groundwork for future directions in structural and mechanistic research on amyloids.

Bibliography

[1] J. Berg, L. Stryer, J. Tymoczko, and G. Gatto, *Biochemistry (8th ed.)*. Macmillan Learning, 2015.

[2] D. Nelson and M. Cox, *Lehninger Principles of Biochemistry: International Edition*. Macmillan Learning, 2021.

[3] N. Louros, J. Schymkowitz, and F. Rousseau, “Mechanisms and pathology of protein misfolding and aggregation,” *Nature Reviews Molecular Cell Biology*, pp. 1–22, 2023.

[4] C. M. Dobson, “Protein folding and misfolding,” *Nature*, vol. 426, no. 6968, pp. 884–890, 2003.

[5] A. L. Fink, “Chaperone-mediated protein folding,” *Physiological reviews*, vol. 79, no. 2, pp. 425–449, 1999.

[6] A. Lilienbaum, “Relationship between the proteasomal system and autophagy,” *International journal of biochemistry and molecular biology*, vol. 4, no. 1, p. 1, 2013.

[7] E. I. Yakupova, L. G. Bobyleva, I. M. Vikhlyantsev, and A. G. Bobylev, “Congo red and amyloids: history and relationship,” *Bioscience reports*, vol. 39, no. 1, p. BSR20181415, 2019.

[8] C. Xue, T. Y. Lin, D. Chang, and Z. Guo, “Thioflavin t as an amyloid dye: fibril quantification, optimal concentration and effect on aggregation,” *Royal Society open science*, vol. 4, no. 1, p. 160696, 2017.

[9] K. L. Morris and L. C. Serpell, “X-ray fibre diffraction studies of amyloid fibrils,” *Amyloid proteins: Methods and protocols*, pp. 121–135, 2012.

[10] T. P. Knowles, M. Vendruscolo, and C. M. Dobson, “The amyloid state and its association with protein misfolding diseases,” *Nature reviews Molecular cell biology*, vol. 15, no. 6, pp. 384–396, 2014.

[11] R. Tycko, “Amyloid polymorphism: structural basis and neurobiological relevance,” *Neuron*, vol. 86, no. 3, pp. 632–645, 2015.

[12] J. N. Buxbaum, A. Dispenzieri, D. S. Eisenberg, M. Fändrich, G. Merlini, M. J. Saraiva, Y. Sekijima, and P. Westermark, “Amyloid nomenclature 2022: update, novel proteins, and recommendations by the international society of amyloidosis (isa) nomenclature committee,” *Amyloid*, vol. 29, no. 4, pp. 213–219, 2022.

[13] F. Folli, S. La Rosa, G. Finzi, A. M. Davalli, A. Galli, E. J. Dick Jr, C. Perego, and R. G. Mendoza, “Pancreatic islet of langerhans’ cytoarchitecture and ultrastructure in normal glucose tolerance and in type 2 diabetes mellitus,” *Diabetes, Obesity and Metabolism*, vol. 20, pp. 137–144, 2018.

[14] H.-L. Zhao, F. M. Lai, P. C. Tong, D.-R. Zhong, D. Yang, B. Tomlinson, and J. C. Chan, “Prevalence and clinicopathological characteristics of islet amyloid in chinese patients with type 2 diabetes,” *Diabetes*, vol. 52, no. 11, pp. 2759–2766, 2003.

[15] M. R. Hayden and S. C. Tyagi, “A” is for amylin and amyloid in type 2 diabetes mellitus,” *Jop*, vol. 2, no. 4, pp. 124–139, 2001.

[16] P. P. Khin, J. H. Lee, and H.-S. Jun, “Pancreatic beta-cell dysfunction in type 2 diabetes,” *European Journal of Inflammation*, vol. 21, p. 1721727X231154152, 2023.

[17] Y. Kiriyama and H. Nochi, “Role and cytotoxicity of amylin and protection of pancreatic islet β-cells from amylin cytotoxicity,” *Cells*, vol. 7, no. 8, p. 95, 2018.

[18] D. L. Hay, M. L. Garelja, D. R. Poyner, and C. S. Walker, "Update on the pharmacology of calcitonin/cgrp family of peptides: Iuphar review 25," *British journal of pharmacology*, vol. 175, no. 1, pp. 3–17, 2018.

[19] D. L. Hay and A. A. Pioszak, "Receptor activity-modifying proteins (ramps): new insights and roles," *Annual review of pharmacology and toxicology*, vol. 56, pp. 469–487, 2016.

[20] N. Tilakaratne, G. Christopoulos, E. T. Zumpe, S. M. Foord, and P. M. Sexton, "Amylin receptor phenotypes derived from human calcitonin receptor/ramp coexpression exhibit pharmacological differences dependent on receptor isoform and host cell environment," *Journal of Pharmacology and Experimental Therapeutics*, vol. 294, no. 1, pp. 61–72, 2000.

[21] M. Calero and M. Gasset, "Fourier transform infrared and circular dichroism spectroscopies for amyloid studies," *Amyloid Proteins: Methods and Protocols*, pp. 129–151, 2005.

[22] J. Adamcik and R. Mezzenga, "Study of amyloid fibrils via atomic force microscopy," *Current Opinion in Colloid & Interface Science*, vol. 17, no. 6, pp. 369–376, 2012.

[23] M. R. Nilsson, "Techniques to study amyloid fibril formation in vitro," *Methods*, vol. 34, no. 1, pp. 151–160, 2004.

[24] C. Goldsbury, U. Baxa, M. N. Simon, A. C. Steven, A. Engel, J. S. Wall, U. Aebi, and S. A. Müller, "Amyloid structure and assembly: insights from scanning transmission electron microscopy," *Journal of structural biology*, vol. 173, no. 1, pp. 1–13, 2011.

[25] J. M. Griffiths, T. T. Ashburn, M. Auger, P. R. Costa, R. G. Griffin, and P. T. Lansbury Jr, "Rotational resonance solid-state nmr elucidates a structural model of pancreatic amyloid," *Journal of the American Chemical Society*, vol. 117, no. 12, pp. 3539–3546, 1995.

[26] J. Madine, E. Jack, P. G. Stockley, S. E. Radford, L. C. Serpell, and D. A. Middleton, "Structural insights into the polymorphism of amyloid-like fibrils formed by region 20- 29 of amylin revealed by solid-state nmr and x-ray fiber diffraction," *Journal of the American Chemical Society*, vol. 130, no. 45, pp. 14990–15001, 2008.

[27] J. T. Nielsen, M. Bjerring, M. D. Jeppesen, R. O. Pedersen, J. M. Pedersen, K. L. Hein, T. Vosegaard, T. Skrydstrup, D. E. Otzen, and N. C. Nielsen, "Unique identification of supramolecular structures in amyloid fibrils by solid-state nmr spectroscopy," *Angewandte Chemie*, vol. 121, no. 12, pp. 2152–2155, 2009.

[28] A. Mascioni, F. Porcelli, U. Ilangovan, A. Ramamoorthy, and G. Veglia, "Conformational preferences of the amylin nucleation site in sds micelles: an nmr study," *Biopolymers: Original Research on Biomolecules*, vol. 69, no. 1, pp. 29–41, 2003.

[29] A. Abedini and D. P. Raleigh, "Incorporation of pseudoproline derivatives allows the facile synthesis of human iapp, a highly amyloidogenic and aggregation-prone polypeptide," *Organic letters*, vol. 7, no. 4, pp. 693–696, 2005.

[30] P. Marek, A. M. Woys, K. Sutton, M. T. Zanni, and D. P. Raleigh, "Efficient microwave-assisted synthesis of human islet amyloid polypeptide designed to facilitate the specific incorporation of labeled amino acids," *Organic letters*, vol. 12, no. 21, pp. 4848–4851, 2010.

[31] S. Luca, W.-M. Yau, R. Leapman, and R. Tycko, "Peptide conformation and supramolecular organization in amylin fibrils: constraints from solid-state nmr," *Biochemistry*, vol. 46, no. 47, pp. 13505–13522, 2007.

[32] P. E. Smith, J. R. Brender, and A. Ramamoorthy, "Induction of negative curvature as a mechanism of cell toxicity by amyloidogenic peptides: the case of islet amyloid polypeptide," *Journal of the American Chemical Society*, vol. 131, no. 12, pp. 4470–4478, 2009.

[33] R. P. R. Nanga, J. R. Brender, S. Vivekanandan, and A. Ramamoorthy, "Structure and membrane orientation of iapp in its natively amidated form at physiological ph in a membrane environment," *Biochimica et Biophysica Acta (BBA)-Biomembranes*, vol. 1808, no. 10, pp. 2337–2342, 2011.

[34] D. C. Rodriguez Camargo, K. Tripsianes, K. Buday, A. Franko, C. Göbl, C. Hartlmüller, R. Sarkar, M. Aichler, G. Mettenleiter, M. Schulz, *et al.*, "The redox environment triggers conformational changes and aggregation of hiapp in type ii diabetes," *Scientific reports*, vol. 7, no. 1, p. 44041, 2017.

[35] P. Krotee, J. A. Rodriguez, M. R. Sawaya, D. Cascio, F. E. Reyes, D. Shi, J. Hattne, B. L. Nannenga, M. E. Oskarsson, S. Philipp, *et al.*, "Atomic structures of fibrillar segments of hiapp suggest tightly mated β-sheets are important for cytotoxicity," *Elife*, vol. 6, p. e19273, 2017.

[36] Q. Cao, D. R. Boyer, M. R. Sawaya, P. Ge, and D. S. Eisenberg, "Cryo-em structure and inhibitor design of human iapp (amylin) fibrils," *Nature structural & molecular biology*, vol. 27, no. 7, pp. 653–659, 2020.

[37] C. Röder, T. Kupreichyk, L. Gremer, L. U. Schäfer, K. R. Pothula, R. B. Ravelli, D. Willbold, W. Hoyer, and G. F. Schröder, "Cryo-em structure of islet amyloid polypeptide fibrils reveals similarities with amyloid-β fibrils," *Nature structural & molecular biology*, vol. 27, no. 7, pp. 660–667, 2020.

[38] R. Gallardo, M. G. Iadanza, Y. Xu, G. R. Heath, R. Foster, S. E. Radford, and N. A. Ranson, "Fibril structures of diabetes-related amylin variants reveal a basis for surface-templated assembly," *Nature Structural & Molecular Biology*, vol. 27, no. 11, pp. 1048–1056, 2020.

[39] Q. Cao, D. R. Boyer, M. R. Sawaya, R. Abskharon, L. Saelices, B. A. Nguyen, J. Lu, K. A. Murray, F. Kandeel, and D. S. Eisenberg, "Cryo-em structures of hiapp fibrils seeded by patient-extracted fibrils reveal new polymorphs and conserved fibril cores," *Nature Structural & Molecular Biology*, vol. 28, no. 9, pp. 724–730, 2021.

[40] D. Li, X. Zhang, Y. Wang, H. Zhang, K. Song, K. Bao, and P. Zhu, "A new polymorphism of human amylin fibrils with similar protofilaments and a conserved core," *Iscience*, vol. 25, no. 12, 2022.

[41] A. Mitra and N. Sarkar, "Sequence and structure-based peptides as potent amyloid inhibitors: A review," *Archives of Biochemistry and Biophysics*, vol. 695, p. 108614, 2020.

[42] T. D. Müller, M. Blüher, M. H. Tschöp, and R. D. DiMarchi, "Anti-obesity drug discovery: advances and challenges," *Nature Reviews Drug Discovery*, vol. 21, no. 3, pp. 201–223, 2022.

[43] P. Cao, A. Abedini, and D. P. Raleigh, "Aggregation of islet amyloid polypeptide: from physical chemistry to cell biology," *Current opinion in structural biology*, vol. 23, no. 1, pp. 82–89, 2013.

[44] S. Edelman, H. Maier, and K. Wilhelm, "Pramlintide in the treatment of diabetes mellitus," *BioDrugs*, vol. 22, pp. 375–386, 2008.

[45] C. Hekman, W. DeMond, T. Dixit, S. Mauch, M. Nuechterlein, A. Stepanenko, J. D. Williams, and M. Ye, "Isolation and identification of peptide degradation products of heat stressed pramlintide injection drug product," *Pharmaceutical research*, vol. 15, pp. 650–658, 1998.

[46] D. F. Kruger and M. A. Gloster, "Pramlintide for the treatment of insulin-requiring diabetes mellitus: rationale and review of clinical data," *Drugs*, vol. 64, pp. 1419–1432, 2004.

[47] C. L. Maikawa, P. C. Chen, E. T. Vuong, L. T. Nguyen, J. L. Mann, A. I. d'Aquino, R. A. Lal, D. M. Maahs, B. A. Buckingham, and E. A. Appel, "Ultra-fast insulin–pramlintide co-formulation for improved glucose management in diabetic rats," *Advanced Science*, vol. 8, no. 21, p. 2101575, 2021.

[48] G. Andersen, R. Eloy, S. Famulla, T. Heise, G. Meiffren, C. Seroussi, M. Gaudier, C. Mégret, Y.-P. Chan, O. Soula, *et al.*, "A co-formulation of pramlintide and insulin a21g (ado09) improves postprandial glucose and short-term control of mean glucose, time in range, and body weight versus insulin aspart in adults with type 1 diabetes," *Diabetes, Obesity and Metabolism*, vol. 25, no. 5, pp. 1241–1248, 2023.

[49] T. Kruse, J. L. Hansen, K. Dahl, L. Schaffer, U. Sensfuss, C. Poulsen, M. Schlein, A. M. K. Hansen, C. B. Jeppesen, C. Dornonville de la Cour, *et al.*, "Development of cagrilintide, a long-acting amylin analogue," *Journal of Medicinal Chemistry*, vol. 64, no. 15, pp. 11183–11194, 2021.

[50] J. P. Frias, S. Deenadayalan, L. Erichsen, F. K. Knop, I. Lingvay, S. Macura, C. Mathieu, S. D. Pedersen, and M. Davies, "Efficacy and safety of co-administered once-weekly cagrilintide 2· 4 mg with once-weekly semaglutide 2· 4 mg in type 2 diabetes: a multicentre, randomised, double-blind, active-controlled, phase 2 trial," *The Lancet*, 2023.

[51] R. Unnikrishnan, R. Pradeepa, S. R. Joshi, and V. Mohan, "Type 2 diabetes: demystifying the global epidemic," *Diabetes*, vol. 66, no. 6, pp. 1432–1442, 2017.

[52] S. B. Charge, E. J. de Koning, and A. Clark, "Effect of ph and insulin on fibrillogenesis of islet amyloid polypeptide in vitro," *Biochemistry*, vol. 34, no. 44, pp. 14588–14593, 1995.

[53] M. Amblard, J.-A. Fehrentz, J. Martinez, and G. Subra, "Methods and protocols of modern solid phase peptide synthesis," *Molecular biotechnology*, vol. 33, pp. 239–254, 2006.

[54] A. Isidro-Llobet, M. Alvarez, and F. Albericio, "Amino acid-protecting groups," *Chemical reviews*, vol. 109, no. 6, pp. 2455–2504, 2009.

[55] T. Wöhr, F. Wahl, A. Nefzi, B. Rohwedder, T. Sato, X. Sun, and M. Mutter, "Pseudo-prolines as a solubilizing, structure-disrupting protection technique in peptide synthesis," *Journal of the American Chemical Society*, vol. 118, no. 39, pp. 9218–9227, 1996.

[56] A. Abedini, G. Singh, and D. P. Raleigh, "Recovery and purification of highly aggregation-prone disulfide-containing peptides: application to islet amyloid polypeptide," *Analytical biochemistry*, vol. 351, no. 2, pp. 181–186, 2006.

[57] Z. L. Almeida and R. M. Brito, "Structure and aggregation mechanisms in amyloids," *Molecules*, vol. 25, no. 5, p. 1195, 2020.

[58] L. M. Miller, M. W. Bourassa, and R. J. Smith, "Ftir spectroscopic imaging of protein aggregation in living cells," *Biochimica et biophysica acta (BBA)-biomembranes*, vol. 1828, no. 10, pp. 2339–2346, 2013.

[59] S.-H. Shim, R. Gupta, Y. L. Ling, D. B. Strasfeld, D. P. Raleigh, and M. T. Zanni, "Two-dimensional ir spectroscopy and isotope labeling defines the pathway of amyloid formation with residue-specific resolution," *Proceedings of the National Academy of Sciences*, vol. 106, no. 16, pp. 6614–6619, 2009.

[60] S.-H. Shim, D. B. Strasfeld, Y. L. Ling, and M. T. Zanni, "Automated 2d ir spectroscopy using a mid-ir pulse shaper and application of this technology to the human islet amyloid polypeptide," *Proceedings of the National Academy of Sciences*, vol. 104, no. 36, pp. 14197–14202, 2007.

[61] L. E. Buchanan, M. Maj, E. B. Dunkelberger, P.-N. Cheng, J. S. Nowick, and M. T. Zanni, "Structural polymorphs suggest competing pathways for the formation of amyloid fibrils that diverge from a common intermediate species," *Biochemistry*, vol. 57, no. 46, pp. 6470–6478, 2018.

[62] S. S. Dicke, M. Maj, C. R. Fields, and M. T. Zanni, "Metastable intermediate during hiapp aggregation catalyzed by membranes as detected with 2d ir spectroscopy," *RSC Chemical Biology*, vol. 3, no. 7, pp. 931–940, 2022.

[63] S. Gonen, "Progress towards cryoem: negative-stain procedures for biological samples," *cryoEM: Methods and Protocols*, pp. 115–123, 2021.

[64] K. M. Yip, N. Fischer, E. Paknia, A. Chari, and H. Stark, "Atomic-resolution protein structure determination by cryo-em," *Nature*, vol. 587, no. 7832, pp. 157–161, 2020.

[65] J. R. Feathers, K. A. Spoth, and J. C. Fromme, "Experimental evaluation of super-resolution imaging and magnification choice in single-particle cryo-em," *Journal of structural biology: X*, vol. 5, p. 100047, 2021.

[66] D. Bhella, "Cryo-electron microscopy: an introduction to the technique, and considerations when working to establish a national facility," *Biophysical reviews*, vol. 11, no. 4, pp. 515–519, 2019.

[67] C. V. Iancu, W. F. Tivol, J. B. Schooler, D. P. Dias, G. P. Henderson, G. E. Murphy, E. R. Wright, Z. Li, Z. Yu, A. Briegel, *et al.*, "Electron cryotomography sample preparation using the vitrobot," *Nature protocols*, vol. 1, no. 6, pp. 2813–2819, 2006.

[68] Y. Cheng, "Single-particle cryo-em—how did it get here and where will it go," *Science*, vol. 361, no. 6405, pp. 876–880, 2018.

[69] S. He and S. H. Scheres, "Helical reconstruction in relion," *Journal of structural biology*, vol. 198, no. 3, pp. 163–176, 2017.

[70] S. H. Scheres, "Amyloid structure determination in relion-3.1," *Acta Crystallographica Section D: Structural Biology*, vol. 76, no. 2, pp. 94–101, 2020.

[71] X. Li, P. Mooney, S. Zheng, C. R. Booth, M. B. Braunfeld, S. Gubbens, D. A. Agard, and Y. Cheng, "Electron counting and beam-induced motion correction enable near-atomic-resolution single-particle cryo-em," *Nature methods*, vol. 10, no. 6, pp. 584–590, 2013.

[72] S. Q. Zheng, E. Palovcak, J.-P. Armache, K. A. Verba, Y. Cheng, and D. A. Agard, "Motioncor2: anisotropic correction of beam-induced motion for improved cryo-electron microscopy," *Nature methods*, vol. 14, no. 4, pp. 331–332, 2017.

[73] A. Rohou and N. Grigorieff, "Ctffind4: Fast and accurate defocus estimation from electron micrographs," *Journal of structural biology*, vol. 192, no. 2, pp. 216–221, 2015.

[74] Z. Huang and P. A. Penczek, "Application of template matching technique to particle detection in electron micrographs," *Journal of Structural Biology*, vol. 145, no. 1-2, pp. 29–40, 2004.

[75] N. Voss, C. Yoshioka, M. Radermacher, C. Potter, and B. Carragher, "Dog picker and tiltpicker: software tools to facilitate particle selection in single particle electron microscopy," *Journal of structural biology*, vol. 166, no. 2, pp. 205–213, 2009.

[76] F. Wang, H. Gong, G. Liu, M. Li, C. Yan, T. Xia, X. Li, and J. Zeng, "Deeppicker: A deep learning approach for fully automated particle picking in cryo-em," *Journal of structural biology*, vol. 195, no. 3, pp. 325–336, 2016.

[77] T. Bepler, A. Morin, M. Rapp, J. Brasch, L. Shapiro, A. J. Noble, and B. Berger, "Positive-unlabeled convolutional neural networks for particle picking in cryo-electron micrographs," *Nature methods*, vol. 16, no. 11, pp. 1153–1160, 2019.

[78] T. Wagner, F. Merino, M. Stabrin, T. Moriya, C. Antoni, A. Apelbaum, P. Hagel, O. Sitsel, T. Raisch, D. Prumbaum, *et al.*, "Sphire-cryolo is a fast and accurate fully automated particle picker for cryo-em," *Communications biology*, vol. 2, no. 1, p. 218, 2019.

[79] P. Emsley, B. Lohkamp, W. G. Scott, and K. Cowtan, "Features and development of coot," *Acta Crystallographica Section D: Biological Crystallography*, vol. 66, no. 4, pp. 486–501, 2010.

[80] P. V. Afonine, B. K. Poon, R. J. Read, O. V. Sobolev, T. C. Terwilliger, A. Urzhumtsev, and P. D. Adams, "Real-space refinement in phenix for cryo-em and crystallography," *Acta Crystallographica Section D: Structural Biology*, vol. 74, no. 6, pp. 531–544, 2018.

[81] P. V. Afonine, B. P. Klaholz, N. W. Moriarty, B. K. Poon, O. V. Sobolev, T. C. Terwilliger, P. D. Adams, and A. Urzhumtsev, "New tools for the analysis and validation of cryo-em maps and atomic models," *Acta Crystallographica Section D: Structural Biology*, vol. 74, no. 9, pp. 814–840, 2018.

[82] S. Chen, J. Li, K. R. Vinothkumar, and R. Henderson, "Interaction of human erythrocyte catalase with air–water interface in cryoem," *Microscopy*, vol. 71, no. Supplement_1, pp. i51–i59, 2022.

[83] J. P. Lomont, K. L. Rich, M. Maj, J.-J. Ho, J. S. Ostrander, and M. T. Zanni, "Spectroscopic signature for stable β-amyloid fibrils versus β-sheet-rich oligomers," *The Journal of Physical Chemistry B*, vol. 122, no. 1, pp. 144–153, 2018.

[84] M. Maj, J. P. Lomont, K. L. Rich, A. M. Alperstein, and M. T. Zanni, "Site-specific detection of protein secondary structure using 2d ir dihedral indexing: a proposed assembly mechanism of oligomeric hiapp," *Chem. Sci.*, vol. 9, no. 2, pp. 463–474, 2018.

[85] D. Kampjut, J. Steiner, and L. A. Sazanov, "Cryo-em grid optimization for membrane proteins," *Iscience*, vol. 24, no. 3, 2021.

[86] K. Klement, K. Wieligmann, J. Meinhardt, P. Hortschansky, W. Richter, and M. Fändrich, "Effect of different salt ions on the propensity of aggregation and on the structure of alzheimer's aβ (1-40) amyloid fibrils," *Journal of molecular biology*, vol. 373, no. 5, pp. 1321–1333, 2007.

[87] A. Abedini and D. P. Raleigh, "The role of his-18 in amyloid formation by human islet amyloid polypeptide," *Biochemistry*, vol. 44, no. 49, pp. 16284–16291, 2005.

[88] J. R. Brender, K. Hartman, R. P. R. Nanga, N. Popovych, R. de la Salud Bea, S. Vivekanandan, E. N. G. Marsh, and A. Ramamoorthy, "Role of zinc in human islet amyloid polypeptide aggregation," *Journal of the American Chemical Society*, vol. 132, no. 26, pp. 8973–8983, 2010.

[89] L.-H. Tu, A. L. Serrano, M. T. Zanni, and D. P. Raleigh, "Mutational analysis of preamyloid intermediates: The role of his-tyr interactions in islet amyloid formation," *Biophysical journal*, vol. 106, no. 7, pp. 1520–1527, 2014.

[90] C. R. Fields, S. S. Dicke, M. K. Petti, M. T. Zanni, and J. P. Lomont, "A different hiapp polymorph is observed in human serum than in aqueous buffer: demonstration of a new method for studying amyloid fibril structure using infrared spectroscopy," *The journal of physical chemistry letters*, vol. 11, no. 15, pp. 6382–6388, 2020.

[91] M. Vasconcelos, M. Azenha, and O. Lage, "Electrochemical evidence of surfactant activity of the hepes ph buffer which may have implications on trace metal availability to culturesin vitro," *Analytical biochemistry*, vol. 241, no. 2, pp. 248–253, 1996.

[92] A. Becke, "Density-functional thermochemistry. iii. the role of exact exchange (1993) j," *Chem. Phys*, vol. 98, p. 5648.

[93] T. Clark, J. Chandrasekhar, G. W. Spitznagel, and P. V. R. Schleyer, "Efficient diffuse function-augmented basis sets for anion calculations. iii. the 3-21+ g basis set for first-row elements, li–f," *Journal of Computational Chemistry*, vol. 4, no. 3, pp. 294–301, 1983.

[94] R. Krishnan, J. S. Binkley, R. Seeger, and J. A. Pople, "Self-consistent molecular orbital methods. xx. a basis set for correlated wave functions," *The Journal of chemical physics*, vol. 72, no. 1, pp. 650–654, 1980.

[95] A. McLean and G. Chandler, "Contracted gaussian basis sets for molecular calculations. i. second row atoms, z= 11–18," *The Journal of chemical physics*, vol. 72, no. 10, pp. 5639–5648, 1980.

[96] G. W. Spitznagel, T. Clark, P. von Ragué Schleyer, and W. J. Hehre, "An evaluation of the performance of diffuse function-augmented basis sets for second row elements, na-cl," *Journal of computational chemistry*, vol. 8, no. 8, pp. 1109–1116, 1987.

[97] C. P. Garnham, R. L. Campbell, V. K. Walker, and P. L. Davies, "Novel dimeric β-helical model of an ice nucleation protein with bridged active sites," *BMC structural biology*, vol. 11, no. 1, pp. 1–12, 2011.

[98] A. Hudait, N. Odendahl, Y. Qiu, F. Paesani, and V. Molinero, "Ice-nucleating and antifreeze proteins recognize ice through a diversity of anchored clathrate and ice-like motifs," *Journal of the American Chemical Society*, vol. 140, no. 14, pp. 4905–4912, 2018.

[99] R. M. Glaeser and B.-G. Han, "Opinion: hazards faced by macromolecules when confined to thin aqueous films," *Biophysics reports*, vol. 3, pp. 1–7, 2017.

[100] M. Zhang, R. Hu, G. Liang, Y. Chang, Y. Sun, Z. Peng, and J. Zheng, "Structural and energetic insight into the cross-seeding amyloid assemblies of human iapp and rat iapp," *The Journal of Physical Chemistry B*, vol. 118, no. 25, pp. 7026–7036, 2014.

[101] H. Wang, Z. Ridgway, P. Cao, B. Ruzsicska, and D. P. Raleigh, "Analysis of the ability of pramlintide to inhibit amyloid formation by human islet amyloid polypeptide reveals a balance between optimal recognition and reduced amyloidogenicity," *Biochemistry*, vol. 54, no. 44, pp. 6704–6711, 2015.

[102] P. Cao, F. Meng, A. Abedini, and D. P. Raleigh, "The ability of rodent islet amyloid polypeptide to inhibit amyloid formation by human islet amyloid polypeptide has important implications for the mechanism of amyloid formation and the design of inhibitors," *Biochemistry*, vol. 49, no. 5, pp. 872–881, 2010.

[103] L. Nielsen, R. Khurana, A. Coats, S. Frokjaer, J. Brange, S. Vyas, V. N. Uversky, and A. L. Fink, "Effect of environmental factors on the kinetics of insulin fibril formation: elucidation of the molecular mechanism," *Biochemistry*, vol. 40, no. 20, pp. 6036–6046, 2001.

[104] B. Morel, L. Varela, A. I. Azuaga, and F. Conejero-Lara, "Environmental conditions affect the kinetics of nucleation of amyloid fibrils and determine their morphology," *Biophysical journal*, vol. 99, no. 11, pp. 3801–3810, 2010.

[105] S. Lövestam, F. A. Koh, B. van Knippenberg, A. Kotecha, A. G. Murzin, M. Goedert, and S. H. Scheres, "Assembly of recombinant tau into filaments identical to those of alzheimer's disease and chronic traumatic encephalopathy," *Elife*, vol. 11, p. e76494, 2022.

[106] R. Abskharon, M. R. Sawaya, D. R. Boyer, Q. Cao, B. A. Nguyen, D. Cascio, and D. S. Eisenberg, "Cryo-em structure of rna-induced tau fibrils reveals a small c-terminal core that may nucleate fibril formation," *Proceedings of the National Academy of Sciences*, vol. 119, no. 15, p. e2119952119, 2022.

[107] L. E. Buchanan, E. B. Dunkelberger, H. Q. Tran, P.-N. Cheng, C.-C. Chiu, P. Cao, D. P. Raleigh, J. J. De Pablo, J. S. Nowick, and M. T. Zanni, "Mechanism of iapp amyloid fibril formation involves an intermediate with a transient β-sheet," *Proceedings of the National Academy of Sciences*, vol. 110, no. 48, pp. 19285–19290, 2013.

[108] C. Weyer, D. G. Maggs, A. A. Young, and O. G. Kolterman, "Amylin replacement with pramlintide as an adjunct to insulin therapy in type 1 and type 2 diabetes mellitus: a physiological approach toward improved metabolic control," *Current pharmaceutical design*, vol. 7, no. 14, pp. 1353–1373, 2001.

[109] Z. Ridgway, C. Eldrid, A. Zhyvoloup, A. Ben-Younis, D. Noh, K. Thalassinos, and D. P. Raleigh, "Analysis of proline substitutions reveals the plasticity and sequence sensitivity of human iapp amyloidogenicity and toxicity," *Biochemistry*, vol. 59, no. 6, pp. 742–754, 2020.

[110] S. H. Scheres, "Relion: implementation of a bayesian approach to cryo-em structure determination," *Journal of structural biology*, vol. 180, no. 3, pp. 519–530, 2012.

[111] D. Liebschner, P. V. Afonine, M. L. Baker, G. Bunkóczi, V. B. Chen, T. I. Croll, B. Hintze, L.-W. Hung, S. Jain, A. J. McCoy, *et al.*, "Macromolecular structure determination using x-rays, neutrons and electrons: recent developments in phenix," *Acta Crystallographica Section D: Structural Biology*, vol. 75, no. 10, pp. 861–877, 2019.

[112] A. K. Paravastu, I. Qahwash, R. D. Leapman, S. C. Meredith, and R. Tycko, "Seeded growth of β-amyloid fibrils from alzheimer's brain-derived fibrils produces a distinct fibril structure," *Proceedings of the National Academy of Sciences*, vol. 106, no. 18, pp. 7443–7448, 2009.

[113] L.-M. Yan, M. Tatarek-Nossol, A. Velkova, A. Kazantzis, and A. Kapurniotu, "Design of a mimic of nonamyloidogenic and bioactive human islet amyloid polypeptide (iapp) as nanomolar affinity inhibitor of iapp cytotoxic fibrillogenesis," *Proceedings of the National Academy of Sciences*, vol. 103, no. 7, pp. 2046–2051, 2006.

[114] H. Wang, A. Abedini, B. Ruzsicska, and D. P. Raleigh, "Rationally designed, nontoxic, nonamyloidogenic analogues of human islet amyloid polypeptide with improved solubility," *Biochemistry*, vol. 53, no. 37, pp. 5876–5884, 2014.

[115] S. J. Wood, R. Wetzel, J. D. Martin, and M. R. Hurle, "Prolines and aamyloidogenicity in fragments of the alzheimer's peptide. beta./a4," *Biochemistry*, vol. 34, no. 3, pp. 724–730, 1995.

[116] Y. Porat, A. Abramowitz, and E. Gazit, "Inhibition of amyloid fibril formation by polyphenols: structural similarity and aromatic interactions as a common inhibition mechanism," *Chemical biology & drug design*, vol. 67, no. 1, pp. 27–37, 2006.

[117] J. F. Aitken, K. M. Loomes, B. Konarkowska, and G. J. Cooper, "Suppression by polycyclic compounds of the conversion of human amylin into insoluble amyloid," *Biochemical Journal*, vol. 374, no. 3, pp. 779–784, 2003.

[118] E. T. Jaikaran, M. R. Nilsson, and A. Clark, "Pancreatic beta-cell granule peptides form heteromolecular complexes which inhibit islet amyloid polypeptide fibril formation," *Biochemical Journal*, vol. 377, no. 3, pp. 709–716, 2004.

[119] R. Hu, M. Zhang, H. Chen, B. Jiang, and J. Zheng, "Cross-seeding interaction between β-amyloid and human islet amyloid polypeptide," *ACS chemical neuroscience*, vol. 6, no. 10, pp. 1759–1768, 2015.

[120] R. Hu, M. Zhang, K. Patel, Q. Wang, Y. Chang, X. Gong, G. Zhang, and J. Zheng, "Cross-sequence interactions between human and rat islet amyloid polypeptides," *Langmuir*, vol. 30, no. 18, pp. 5193–5201, 2014.